

Autonomous Ground Vehicle Path Planning in Urban Environments Using GNSS and Cellular Signals Reliability Maps: Models and Algorithms

SONYA RAGOTHAMAN , Member, IEEE
Aerospace Corporation, El Segundo, CA, USA

MAHDI MAAREF
ZAHER M. KASSAS , Senior Member, IEEE
University of California Irvine, CA, USA

In this article, autonomous ground vehicle (AGV) path planning is considered. The AGV is assumed to be equipped with receivers capable of producing pseudorange measurements to overhead global navigation satellite systems (GNSS) satellites and to cellular base stations in its environment. Parameters of the cellular pseudoranges related to the transmitter clock bias are estimated in an initialization step in an open-sky environment. The AGV fuses these pseudoranges to produce an estimate about its own states. The AGV is also equipped with a three-dimensional building map of the environment. Starting from a known starting point, the AGV desires to reach a known target point by taking the shortest distance, while minimizing the AGV's position estimation error and guaranteeing that the AGV's position estimation uncertainty is below a desired threshold. Toward this objective, a so-called signal reliability map is first generated, which provides information about regions where large errors due to poor GNSS line-of-sight or cellular signal multipath are expected. The vehicle uses the signal reliability map to calculate the position mean-squared error (MSE). An analytical expression for the AGV's state estimates is

Manuscript received August 12, 2019; revised February 8, 2020, September 28, 2020, and November 19, 2020; released for publication November 30, 2020. Date of publication January 26, 2021; date of current version June 9, 2021.

DOI. No. 10.1109/TAES.2021.3054690

Refereeing of this contribution was handled by O. Osechas.

This work was supported in part by the Office of Naval Research (ONR) under Grant N00014-19-1-2613 and in part by the National Science Foundation (NSF) under Grant 1929571 and Grant 1929965.

Authors' addresses: Sonya Ragothaman was with the Department of Electrical and Computer Engineering, University of California, Riverside, CA 90245 USA. She is now with Aerospace Corporation, El Segundo, CA 90245 USA, E-mail: (sonya.ragothaman@gmail.com). Maaref Maaref and Zaher (Zak) M. Kassas are with Department of Mechanical and Aerospace Engineering, University of California, Irvine, CA 90245 USA, E-mail: (mmaaref@uci.edu; zkassas@ieee.org). (*Corresponding author:* Zaher (Zak) M. Kassas.)

0018-9251 © 2021 IEEE

derived, which is used to find an upper bound on the position bias due to multipath. An optimal path planning generation approach, which is based on Dijkstra's algorithm, is developed to optimize the AGV's path while minimizing the path length and position MSE, subject to keeping the position estimation uncertainty and position estimation bias due to multipath below desired thresholds. The path planning approach yields the optimal path together with a list of feasible paths and reliable GNSS satellites and cellular base stations to use along these paths.

NOMENCLATURE

α_p	Node that proceeds α along a path.
α_{spur}	Spur node.
$a_i(x)$	Complex amplitude of signal path x and LTE symbol i .
$b_{m,p}$	Multipath bias assigned to signal reliability map.
c	Speed of light.
$d(g)$	Cost along the path from s to g .
d_{LOS}	Length of the LOS path.
$\text{dist}(p)$	Distance represented by location p .
$f(\beta, \alpha)$	Path planning weight assigned to the edge between nodes α and β .
$f_1(\beta, \alpha)$	Path planning weight assigned to the edge between nodes α and β .
$f_2(\mathcal{A}^z)$	Path planning weight assigned edges along the z th path \mathcal{A}^z .
g	Target node.
$h_i(t)$	Channel impulse response at time t and LTE symbol i .
i	LTE symbol.
$\bar{\lambda}_{\max}$	Threshold for position uncertainty.
\bar{r}_{\max}	Upper bound on position bias.
β_p	Node that proceeds β along a path.
χ_m	$\triangleq \chi_{1,m}(i) + \chi_{2,m}(i)$, multipath interference.
$\delta t_{\text{cell},m}$	m th cellular clock bias.
$\delta t_{r_{\text{gnss}}}$	GNSS receiver clock bias.
$\delta t_{r_{\text{cell}}}$	Cellular receiver clock bias.
$\delta t_{\text{iono},n}$	Ionospheric delay.
$\delta t_{\text{tropo},n}$	Tropospheric delay.
$\delta t_{r_{\text{cell}}}$	Experiment cellular receiver clock bias.
$\delta t_{r_{\text{gnss}}}$	Experiment GNSS receiver clock bias.
δt_r	Receiver clock bias.
ϵ_m	Constant bias between cellular clock biases.
η_{\max}	Pseudorange bias threshold.
η_m	Weighted pseudorange bias threshold.
$\gamma(g)$	A path from nodes s to g .
γ_{rootpath}	A root path from s to α_{spur} .
γ_{spur}	A spur path from α_{spur} to g .
$\gamma(g)$	A path from nodes s to g .
κ	Threshold for amplitude of received path.
$\lambda_{\max}(p, t)$	Maximum eigenvalue used in path planning.
\mathcal{G}	$= (\iota, \omega)$, directed graph with ι nodes and ω edges.
$\mathcal{M}_{\text{cell}}$	Sequence of all cellular signal reliability maps.
$\mathcal{M}_{\text{gnss}_n}$	Signal reliability maps for the n th satellite.
$\mathcal{M}_{\text{gnss}}$	Sequence of all satellite signal reliability maps.
\mathcal{P}	Set of all paths from start to target.

$\mathcal{T}_{\text{gnss},n,p}$	Sequence of time intervals for the n th satellite and the p th location.	P	Number of locations in the reliability map.
\mathcal{A}	Set of ζ shortest paths.	$P(\beta, \alpha)$	Location indices from nodes β to α .
\mathcal{B}	Set of candidate ζ shortest paths.	p_g	Target position index.
\mathbf{B}	Partition of \mathbf{H} corresponding to the clock states.	p_s	Start position index.
$\bar{\mathbf{B}}$	$= \mathbf{R}_a^{-T} \mathbf{B}$.	S	Evaluated edges.
Γ	$= (\mathbf{B}^T \bar{\mathbf{B}})^{-1}$.	s	Start node.
$\tilde{\mathbf{G}}$	$= (\mathbf{I} - \bar{\mathbf{B}} \Gamma \bar{\mathbf{B}}^T) \bar{\mathbf{G}}$.	t	Time.
\mathbf{G}	Partition of \mathbf{H} corresponding to the position states.	T_τ	Number of time intervals.
$\tilde{\mathbf{G}}$	$= \mathbf{R}_a^{-T} \mathbf{G}$.	$t_{\text{end},p,\tau}$	End time for time interval.
\mathbf{G}_{cell}	Partition of \mathbf{G} corresponding to the cellular measurements.	$t_{\text{start},p,\tau}$	Start time for time interval.
\mathbf{G}_{gnss}	Partition of \mathbf{G} corresponding to the satellite measurements.	T_s	Sampling interval.
\mathbf{H}	Measurement Jacobian, $= [\mathbf{G}, \mathbf{B}]$.	V	Unvisited nodes.
\mathbf{R}	Measurement noise covariance.	$v_{\epsilon,m}$	$\sim \mathcal{N}(0, \sigma_{\epsilon,m}^2)$.
\mathbf{R}_a	Cholesky factor of \mathbf{R} .	v_{AGV}	AGV constant speed.
π	Path from start to target location.	$v_{\text{cell},m}$	$\sim \mathcal{N}(0, \sigma_{\text{cell},m}^2)$.
$\rho_{\text{cell},m}$	Cellular pseudorange measurement.	$v'_{\text{cell},m}$	$\triangleq v_{\text{cell},m} - v_{\epsilon,m}, \sim \mathcal{N}(0, \sigma_{\text{cell},m}^2 + \sigma_{\epsilon,m}^2)$.
$\rho_{\text{gnss},n}$	Satellite pseudorange measurement.	$v_{\text{gnss},n}$	$\sim \mathcal{N}(0, \sigma_{\text{gnss},n}^2)$.
$\tau_i(x)$	Path delay between the x th impulse to the LOS path.	X	Number of impulses.
\tilde{e}_θ	Symbol timing error.	$z_{\text{init},m}$	Modified cellular measurement for initialization.
$\bar{\mathbf{b}}$	$= \mathbf{R}_a^{-T} \mathbf{b}$.		
$\Delta \mathbf{r}'_r$	Unbiased position error.		
$\Delta \mathbf{x}'_r$	$= [\Delta \mathbf{r}'_r^T, c \Delta \mathbf{t}'^T]^T$, unbiased error state.		
$\Delta \mathbf{x}_r$	State estimation error.		
Δz_r	Residual vector.		
$\Delta \mathbf{z}'_r$	Unbiased measurement error vector.		
\mathbf{b}	Vector of deterministic measurement biases.		
$\mathbf{r}_{\text{cell},m}$	Position of the m th cellular transmitter.		
$\mathbf{r}_{\text{gnss},n}$	Position of the n th satellite transmitter.		
$r_{r,\text{err}}$	Position bias.		
\mathbf{r}_r	Vehicles 3-D position.		
\mathbf{v}	Vector of measurement noises.		
$\mathbf{x}_{r,\text{err}}$	$= [\mathbf{r}_{r,\text{err}}^T, c \delta t_{\text{err}}^T]^T$, state bias.		
\mathbf{x}_r	AGV state vector.		
$\mathbf{z}_{\text{cell},m}$	Modified cellular pseudorange measurement.		
$\mathbf{z}_{\text{gnss},n}$	Modified satellite pseudorange measurement.		
\mathbf{z}_r	Measurement vector.		
ξ	Correlator spacing in the LTE receiver tracking loop.		
ζ	Number of paths in the search space.		
A	Signal power.		
K	Number of measurements used in cellular measurement initialization.		
L	Number of subcarrier symbols in the pilot sequence.		
m	$= 1, \dots, M$, cellular transmitter index.		
M	Number of cellular base stations in the environment.		
\bar{M}	Number of reliable cellular measurements.		
$\text{MSE}(p, t)$	Position MSE used in path planning.		
n	$= 1, \dots, N$, satellite transmitter index.		
N	Number of GNSS satellites in the environment.		
\bar{N}	Number of reliable GNSS measurements.		
p	Location index.		

I. INTRODUCTION

Autonomous ground vehicles (AGVs) are predicted to improve the quality of life by automating the monotonous task of driving, while reducing crash fatalities due to human error. Considering the breadth of applications AGVs could revolutionize (e.g., cargo delivery, taxi services, emergency response, intelligent farming, etc.), a myriad number of corporations have been investing in AGV enabling technologies [1].

In light of recent tragedies [2], it is evident that AGVs need extremely reliable sensing and navigation systems. Virtually all current vehicular navigation systems rely on global navigation satellite systems (GNSS). While GNSS provide an accurate position estimate with respect to a global frame, its signals are unreliable for the safety critical application of autonomous driving. On one hand, GNSS signals are susceptible to unintentional interference, intentional jamming, and malicious spoofing [3]. On the other hand, GNSS signals are severely attenuated in deep urban canyons. Urban high-rise structures block, shadow, and reflect signals from GNSS satellites. This makes locales at which reliable and accurate GNSS position estimates are achievable to be rather spotty in urban environments [4].

To overcome the limitations of GNSS, current vehicular navigation systems fuse GNSS receivers with a suite of sensor-based technologies (e.g., inertial measurement unit, lidar, and camera). These dead reckoning type sensors need an external aiding source to account for their accumulated error, only provide local position estimates, may not properly function in all environments (e.g., fog, snow, rain, dust, etc.), and are still susceptible to malicious attacks [5].

Signal-based technologies alleviate some of the shortcomings of sensor-based technologies and provide a global position estimate, but some require installing dedicated infrastructure (e.g., pseudolites [6]), while others produce a

coarse position estimate (e.g., digital television signals [7]). Among signal-based technologies, cellular signals are very attractive in urban environments due to their inherent attributes [8], which include the following.

- 1) Reception at high carrier-to-noise ratio (C/N_0): A C/N_0 between 55 and 80 dB-Hz has been observed in urban environments.
- 2) Abundance: Numerous stations corresponding to different cellular providers exist in urban environments.
- 3) Favorable geometric configurations: Cells in cellular networks are designed to minimize interference between stations.

Recent work have demonstrated meter-level accurate navigation with cellular signals on ground vehicles [9]–[14] and centimeter-level accurate navigation on aerial vehicles [15], [16]. In addition to utilizing cellular measurements, AGVs can employ path planning to improve positioning. The objective of path planning, also known as motion planning or trajectory generation, is to optimize a path over a defined objective function (e.g., path length, path duration, position uncertainty, etc.).

This article and its sequel consider the following problem, originally defined in [17]. An AGV is equipped with receivers capable of producing pseudoranges to overhead GNSS satellites and to cellular long-term evolution (LTE) base stations in its environment. From a known starting point, given a 3-D building map, the AGV desires to reach a known target point by taking the shortest distance while minimizing the AGV's position estimation error and guaranteeing that the AGV's position estimation uncertainty is below a desired threshold. This article focuses on modeling, analytical derivations, and algorithm development, while the sequel paper [18] presents comprehensive simulation and experimental results for different realistic scenarios to evaluate the accuracy and efficacy of the proposed approach on a ground vehicle navigating in a deep urban environment.

The contributions of this article are fourfold. First, this article introduces GNSS and cellular signal reliability maps, which store information about areas where GNSS satellites have unobstructed line-of-sight (LOS) and areas where cellular pseudorange measurements produce acceptable errors due to multipath (i.e., below a certain threshold). Second, this article proposes a method for calculating the position mean-squared error (MSE), which measures the expected quality of the position estimate at different locations and time along the road network. Third, this article derives an analytical expression for the position bias due to multipath, which is shown to be parameterized by a bound on the pseudorange bias and the largest eigenvalue of the position estimation error covariance. Fourth, this article proposes a path planning method that is based on Dijkstra's algorithm, which considers path length, position MSE, and the largest eigenvalue of the position estimation error covariance.

This article is organized as follows. Section II overviews related work in path planning. Section III describes the AGV path planning problem. Section IV describes the GNSS and

cellular measurement models and estimation framework used in this article. Section V presents methods to generate GNSS and cellular signal reliability maps. Section VI shows how to calculate the position MSE from signal reliability maps, and finds an upper bound on the position bias. Section VII describes optimal path planning generation, which considers the path length, position MSE, and upper bound on the position bias. Finally, Section VIII concludes this article.

II. RELATED WORK

Path planning has been extensively studied in different contexts. In robotics simultaneous localization and mapping (SLAM), path planning has been considered to steer the robot in the most informative direction [19] or to minimize the probability of becoming lost [20]. In intelligent vehicles, predictive and multirate reactive planning was considered by using the vehicle dynamics, position uncertainty, and obstacle volume to derive Lagrange–Euler equations and potential fields [21]. Also in intelligent vehicles, a partially observable Markov decision process (POMDP) was used for belief state planning to account for uncertainty from noise in sensor data and the intentions of human drivers [22]. In traffic management, the probability of arriving on-time in a bus network under travel time uncertainty was solved using path planning [23]. In target tracking, path planning was considered to minimize the time between observations of a target made by several mobile unmanned aerial vehicles (UAVs) [24]. UAV path planning was considered in [25] to account for map, location, and sensing uncertainty, while it was considered in [26] to generate collision avoidance paths using a Markov decision process. In marine vehicles, path planning was considered to localize underwater acoustic transponders [27]. In navigation via signals of opportunity, path planning was considered to maximize the information gathered from ambient signals to yield accurate positioning and timing [28].

Path planning has been also proposed to reduce position errors from GNSS signals. These position errors can be predicted based on GNSS signal power and availability prediction, proposed in [29]–[35]. In [36], a UAV was steered toward higher received global positioning system (GPS) signal-to-noise ratio (SNR) to improve the signal quality for positioning. In [37] and [38], path planning was considered to account for uncertainty in GNSS-derived position estimates by using dilution of precision (DOP) of GNSS satellites. Stochastic reachability analysis was used in [39] to optimize over DOP-based position uncertainty for a UAV while also avoiding collisions. In [40], predictions of DOP-based position uncertainty and multipath errors for GNSS signals were considered to define and calculate quality of service (QoS) parameters (e.g., availability, accuracy, reliability, and continuity) along a given route. A localization error map, with GPS positioning errors due to multipath-induced biases, was used for UAV path planning in [41]. In [42], a UAV ignored measurements with high multipath-induced biases and avoided areas with poor DOP,

predicted by so-called obstructed LOS volumes and multipath volumes.

The aforementioned metrics can be used for path planning to reduce position errors for an AGV that utilizes GNSS and cellular signals. However, additional challenges need to be accounted for when fusing cellular signals alongside GNSS signals for AGV navigation. Due to the terrestrial nature and modulation scheme of cellular signals, their received signals in urban environments suffer from LOS blockage and severe multipath compared to GNSS signals [43]. This induces errors in cellular navigation observables (pseudoranges), which contaminate the position estimate, jeopardizing the safe operation of AGVs. Though multipath mitigation techniques for navigation with cellular signals in the presence of the LOS signal have been proposed [44], [45], an AGV could further improve the positioning by optimizing its path for small positioning errors.

In this article, path planning is used to guarantee a desired level of accuracy, by choosing a path that yields acceptable DOP-based uncertainty and multipath-induced biases through the position MSE metric. In contrast to the cost function in [41], which accounts for multipath-induced bias, the position MSE cost function proposed in this article also accounts for other sources of error through DOP-based uncertainty. Also, this article explicitly considers orthogonal frequency-division multiplexing (OFDM) signal models in multipath calculations. Furthermore, in contrast to the path planning algorithm in [42], which uses the predicted positioning error in the path planning constraints, this article uses positioning error in the cost function and the constraints.

This article demonstrates the feasibility of using path planning to improve positioning using GNSS and cellular measurements. For practicality, this work can be combined with more sophisticated techniques for GNSS positioning with 3-D maps [46], integrity monitoring notions [47], map matching [48], and sensor fusion and filtering techniques.

III. PROBLEM DESCRIPTION

This article considers the following problem. An AGV drives in an urban environment. The AGV is equipped with receivers capable of producing pseudorange measurements on GNSS satellites and nearby cellular base stations. The AGV uses these pseudorange measurements to estimate the vehicles' 3-D position, AGV-mounted receiver's clock bias, and the clock bias of the cellular base stations. The AGV desires to reach a target location by taking the shortest possible path while guaranteeing that the uncertainty about its own position estimate is below a specified threshold (e.g., for safety concerns). A trajectory that satisfies this objective is generated either locally (i.e., within the AGV's processor) or at a cloud-hosted path planning generator. The path planning generator uses a 3-D building map of the environment to generate a so-called signal reliability map. The signal reliability map is a spatiotemporal map of the environment that measures the expected accuracy from

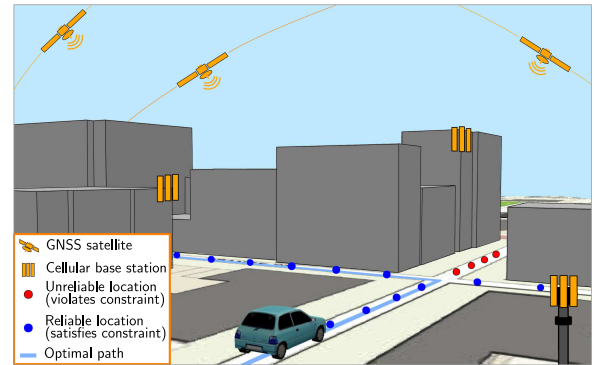


Fig. 1. Depiction of an AGV navigating with GNSS and cellular signals. Here, the red circles represent locations where GNSS and cellular signals are unreliable (i.e., the position estimate produced with such signals will violate position bias and uncertainty constraints) due to limited LOS to GNSS satellites and/or large cellular multipath errors. The blue circles represent locations where GNSS and cellular signals are reliable. The proposed framework generates the optimal blue trajectory, which satisfies the constraints while minimizing the distance traveled between the start and target positions together with minimizing the position MSE. This figure was obtained with ArcGIS [49].

using GNSS and cellular signals to produce an estimate of the AGV's state. For GNSS signals, the signal reliability map is spatiotemporal, and specifies the GNSS satellites to which the AGV would have a blocked LOS for different locations at different times in the environment. For cellular signals, the signal reliability map is a spatial map specifying the expected pseudorange bias due to multipath. The signal reliability maps are used to calculate the position MSE at each location, which in turn is used to generate an optimal path for the AGV to follow. This path is generated by minimizing the total distance traveled and MSE, while guaranteeing that the bias in the position estimate due to multipath is below a desired threshold as well as ensuring that the maximum position uncertainty is below a desired limit. The thresholds can be chosen by the user (e.g., based on the lane-level accuracy). In addition, the path generator produces a table of reliable GNSS satellites and cellular base stations along the optimal path for the AGV to use as it traverses the optimal path. The path planning generator also outputs other feasible paths the AGV could take. These sub-optimal, yet feasible paths could be useful, should the AGV choose to not follow the optimal path, e.g., to avoid traffic jams and road blockages due to construction or emergency. Fig. 1 depicts the objective of the optimal path planning generator. Here, the red circles on the street represent locations that violate the user-specified constraints (position bias or position uncertainty exceeding their respective thresholds).

Fig. 2 illustrates a flowchart of the optimal path generator framework developed in this article.

IV. MODEL DESCRIPTION AND ESTIMATION ALGORITHM

A. AGV-Mounted Receiver States

The AGV receives signals from M spatially stationary cellular base stations. It is assumed that the coordinates

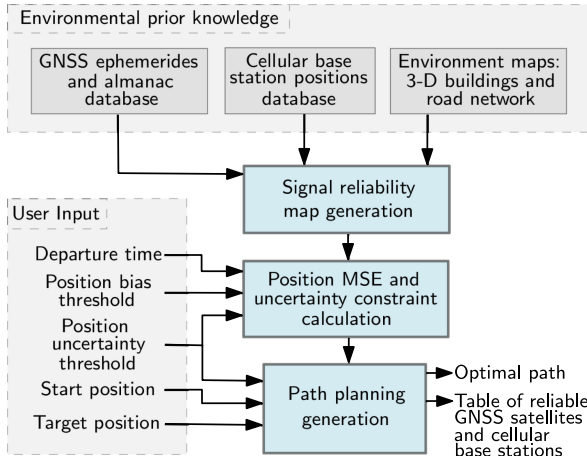


Fig. 2. Flowchart of the proposed path planning generator. The path planning generator is assumed to have knowledge of GNSS orbital data, cellular base station positions, and 3-D environment map. The user inputs are: departure time, start position, target position, position bias threshold, and position uncertainty threshold. The thresholds are used as constraints to find the optimal path. The outputs of the path planning generator are the optimal path and a table of reliable GNSS satellites and cellular base stations to use along the optimal path.

of the cellular base stations are known *a priori* (e.g., via radio mapping or satellite images [50], [51]) and are stored locally on the AGV or on a cloud-hosted database. The 3-D position of the m th cellular base station is denoted $\mathbf{r}_{\text{cell},m} \triangleq [x_{\text{cell},m}, y_{\text{cell},m}, z_{\text{cell},m}]^T$ in the Earth-centered Earth-fixed (ECEF) coordinate frame. The AGV also receives signals from N GNSS satellites with known positions. The 3-D position of the n th GNSS satellite is denoted as $\mathbf{r}_{\text{gnss},n} \triangleq [x_{\text{gnss},n}, y_{\text{gnss},n}, z_{\text{gnss},n}]^T$ in the ECEF coordinate frame.

The unknown states include the vehicle's 3-D position $\mathbf{r}_r \triangleq [x_r, y_r, z_r]^T$ in the ECEF coordinate frame, the AGV-mounted receiver's clock bias δt_r , and the clock bias of the M cellular base stations $\{\delta t_{\text{cell},m}\}_{m=1}^M$. The cellular LTE technical specification requires transmitters in neighboring cells to be synchronized in phase up to $10 \mu\text{s}$ [52]. The cellular base station clock bias is a time-varying state, but synchronization between the clock biases can be exploited. Many cellular providers synchronize nearby base stations in a much tighter fashion as was demonstrated over a 24-h period in recent experimental studies [15], [53]. This synchronization will be exploited in the proposed framework to minimize the number of states that will be estimated. Specifically, only the clock bias of one of the base stations will be estimated (referred to as the first base station, without loss of generality). The clock bias of the other cellular base stations will be expressed as deviations from the clock bias of the first base station. The model of such deviation and the estimation algorithm will be discussed in the following subsections.

B. AGV Measurements

The AGV-mounted receiver makes pseudorange measurements to the N GNSS satellites. The n th GNSS

pseudorange measurement is modeled as

$$\rho_{\text{gnss},n}(k) = \|\mathbf{r}_r(k) - \mathbf{r}_{\text{gnss},n}(k)\|_2 + c \cdot [\delta t_r(k) - \delta t_{\text{gnss},n}(k)] + c\delta t_{\text{iono},n}(k) + c\delta t_{\text{tropo},n}(k) + v_{\text{gnss},n}(k)$$

where c is the speed of light; $\delta t_{\text{iono},n}$ and $\delta t_{\text{tropo},n}$ are known ionospheric and tropospheric delays, respectively; and $\delta t_{\text{gnss},n}$ is the known satellite clock bias. The model coefficients for the terms $\mathbf{r}_{\text{gnss},n}$, $\delta t_{\text{iono},n}$, and $\delta t_{\text{gnss},n}$ are transmitted in the satellite's navigation message. The term $\delta t_{\text{tropo},n}$ is found using the Hopfield model [54]. The term $v_{\text{gnss},n}$ is the measurement noise, which is modeled as a zero-mean white Gaussian random sequence with variance $\sigma_{\text{gnss},n}^2$. The measurements noise across different satellites $\{v_{\text{gnss},n}\}_{n=1}^N$ are assumed to be independent. The n th GNSS pseudorange measurement is modified by subtracting the known $\delta t_{\text{iono},n}$, $\delta t_{\text{tropo},n}$, and $c\delta t_{\text{gnss},n}$ to yield [54]

$$\begin{aligned} z_{\text{gnss},n} &\triangleq \rho_{\text{gnss},n} - c\delta t_{\text{iono},n} - c\delta t_{\text{tropo},n} + c\delta t_{\text{gnss},n} \\ &= \|\mathbf{r}_r - \mathbf{r}_{\text{gnss},n}\|_2 + c\delta t_r + v_{\text{gnss},n}. \end{aligned} \quad (1)$$

Multipath interference and non-line-of-sight (NLOS) errors are not included in the measurement model because NLOS measurements are not used, and the GNSS receiver mitigates multipath when the LOS signal is present.

The AGV-mounted receiver also makes pseudorange measurements to the M cellular base stations. The m th cellular pseudorange measurement is modeled as [55]

$$\rho_{\text{cell},m}(k) = \|\mathbf{r}_r(k) - \mathbf{r}_{\text{cell},m}\|_2 + c \cdot [\delta t_r(k) - \delta t_{\text{cell},m}(k)] + v_{\text{cell},m}(k)$$

where $v_{\text{cell},m}$ is the measurement noise, which is modeled as a zero-mean white Gaussian sequence with variance $\sigma_{\text{cell},m}^2$. The measurement noise across different cellular base stations $\{v_{\text{cell},m}\}_{m=1}^M$ are assumed to be independent. The model assumes that there is no multipath-induced bias. In the case that there is multipath, a bias is introduced, causing a mismatch with the model. The subsequent sections address bounding the pseudorange error, thereby, bounding the induced bias in the position estimate.

By exploiting the synchronization between nearby cellular base stations, the transmitter clock bias of the m th cellular measurement can be expressed as

$$c\delta t_{\text{cell},m}(k) = c\delta t_{\text{cell},1}(k) + \epsilon_m + v_{\epsilon,m}(k) \quad (2)$$

for $m = 2, \dots, M$, where ϵ_m is a deterministic constant bias, and $v_{\epsilon,m}$ is approximated as a zero-mean white noise sequence with variance $\sigma_{\epsilon,m}^2$. This model is valid over relatively short periods of time [53], but more sophisticated models capturing the long-term behavior of synchronization, or lack of, can be used [11], [15], [56], [57]. For all cellular measurements other than the first cellular measurement, the m th cellular pseudorange can be rewritten in terms of $c\delta t_{\text{cell},1}$, namely

$$\begin{aligned} \rho_{\text{cell},m}(k) &= \|\mathbf{r}_r(k) - \mathbf{r}_{\text{cell},m}\|_2 + c\delta t_r(k) - c\delta t_{\text{cell},1}(k) \\ &\quad - \epsilon_m + v'_{\text{cell},m}(k) \end{aligned} \quad (3)$$

for $m = 2, \dots, M$, where $v'_{\text{cell},m} \triangleq v_{\text{cell},m} - v_{\epsilon,m}$ is a zero-mean white noise sequence with variance $\sigma_{\text{cell},m}^2 + \sigma_{\epsilon,m}^2$.

Finally, using (2), the cellular pseudorange measurement (3) to the M cellular base stations is modified according to

$$\begin{aligned} z_{\text{cell},1}(k) &= \|\mathbf{r}_r(k) - \mathbf{r}_{\text{cell},1}\|_2 + c[\delta t_r(k) - \delta t_{\text{cell},1}(k)] \\ &\quad + v_{\text{cell},1}(k) \\ z_{\text{cell},m}(k) &\triangleq \rho_{\text{cell},m}(k) + \epsilon_m \\ &= \|\mathbf{r}_r(k) - \mathbf{r}_{\text{cell},m}\|_2 + c[\delta t_r(k) - \delta t_{\text{cell},1}(k)] \\ &\quad + v'_{\text{cell},m}(k) \end{aligned}$$

for $m = 2, \dots, M$. The next subsection describes an estimation procedure for ϵ_m and $\sigma_{\epsilon,m}^2$.

C. Estimation of Cellular Measurement Clock Bias Perturbations

The perturbation parameters of the m th cellular clock bias from the first cellular clock bias [cf., (2)], namely, the constant bias ϵ_m and the variance $\sigma_{\epsilon,m}^2$ can be estimated by the AGV-mounted receiver locally or assumed to be available from a cloud-hosted database. To estimate the constant bias ϵ_m and variance $\sigma_{\epsilon,m}^2$, the measurements are differenced according to

$$\begin{aligned} \rho_{\text{cell},1}(k) - \rho_{\text{cell},m}(k) &= \|\mathbf{r}_r(k) - \mathbf{r}_{\text{cell},1}\|_2 \\ &\quad - \|\mathbf{r}_r(k) - \mathbf{r}_{\text{cell},m}\|_2 + \epsilon_m \\ &\quad + v_{\text{cell},1}(k) - v'_{\text{cell},m}(k). \end{aligned} \quad (4)$$

$\rho_{\text{cell},1}(k)$ can be swapped with another cellular measurement without loss of generality. It is assumed that the differencing operation in (4) is performed in an open area where \mathbf{r}_r is accurately estimated (e.g., while the AGV is initially stationary with clear LOS to GNSS satellites). Subsequently, define the measurement

$$\begin{aligned} z_{\text{init},m}(k) &\triangleq \rho_{\text{cell},1}(k) - \rho_{\text{cell},m}(k) - \|\mathbf{r}_r(k) - \mathbf{r}_{\text{cell},1}\|_2 \\ &\quad + \|\mathbf{r}_r(k) - \mathbf{r}_{\text{cell},m}\|_2 \\ &= \epsilon_m + v_{\text{cell},1}(k) - v_{\text{cell},m}(k) + v_{\epsilon,m}(k). \end{aligned}$$

Assuming the measurement noise to be ergodic (i.e., the ensemble average equals the time average), ϵ_m and $\sigma_{\epsilon,m}^2$ can be estimated using a sample mean and a sample variance over K measurements, namely

$$\begin{aligned} \hat{\epsilon}_m &= \frac{1}{K} \sum_{k=1}^K z_{\text{init},m}(k) \\ \hat{\sigma}_{\epsilon,m}^2 &= \left[\frac{1}{K-1} \sum_{k=1}^K [z_{\text{init},m}(k) - \hat{\epsilon}_m]^2 \right] - \sigma_{\text{cell},1}^2 - \sigma_{\text{cell},m}^2. \end{aligned}$$

The value of K can be a fixed value chosen prior to the initialization, or can be determined during initialization by increasing K until the sample mean and variance converge. In practice, the value of K depends on the batch size for which (2) holds. Experimentally, it was observed that the sample mean and variance converged in around 0.5 s with

measurements at a sampling time $T = 0.1$ s (i.e., $K \approx 50$ samples).

D. Estimation of AGV States

The AGV's state vector defined as $\mathbf{x}_r \triangleq [\mathbf{r}_r^\top, c\delta t_r, c\delta t_{\text{cell},1}]^\top$ is estimated from the measurement vector $\mathbf{z}_r \triangleq [z_{\text{gnss},1}, \dots, z_{\text{gnss},N}, z_{\text{cell},1}, \dots, z_{\text{cell},M}]^\top$ through a weighted nonlinear least-squares (WNLS) estimator.

The measurement Jacobian used in the WNLS estimator is $\mathbf{H} \triangleq [\mathbf{G}, \mathbf{B}]$, where

$$\begin{aligned} \mathbf{G} &\triangleq \left[\mathbf{G}_{\text{gnss}}^\top, \mathbf{G}_{\text{cell}}^\top \right]^\top \\ \mathbf{G}_{\text{gnss}} &\triangleq \begin{bmatrix} \frac{\mathbf{r}_r^\top - \mathbf{r}_{\text{gnss},1}^\top}{\|\mathbf{r}_r - \mathbf{r}_{\text{gnss},1}\|_2} \\ \vdots \\ \frac{\mathbf{r}_r^\top - \mathbf{r}_{\text{gnss},N}^\top}{\|\mathbf{r}_r - \mathbf{r}_{\text{gnss},N}\|_2} \end{bmatrix}, \quad \mathbf{G}_{\text{cell}} \triangleq \begin{bmatrix} \frac{\mathbf{r}_r^\top - \mathbf{r}_{\text{cell},1}^\top}{\|\mathbf{r}_r - \mathbf{r}_{\text{cell},1}\|_2} \\ \vdots \\ \frac{\mathbf{r}_r^\top - \mathbf{r}_{\text{cell},M}^\top}{\|\mathbf{r}_r - \mathbf{r}_{\text{cell},M}\|_2} \end{bmatrix}, \end{aligned}$$

and

$$\mathbf{B} \triangleq \begin{bmatrix} \mathbf{1}_{N \times 1} & \mathbf{0}_{N \times 1} \\ \mathbf{1}_{M \times 1} & -\mathbf{1}_{M \times 1} \end{bmatrix} \quad (5)$$

where $\mathbf{1}$ and $\mathbf{0}$ are matrices of ones and zeros, respectively. The \mathbf{G} matrix is the partition of the measurement Jacobian corresponding to the AGV position states, and can be found in navigation textbooks [54]. The \mathbf{B} matrix is the partition of the measurement Jacobian corresponding to the clock bias states.

In some cases, the GNSS and cellular receiver clocks are not synchronized, which implies that each receiver had a different clock bias, denoted as δt_{gnss} and δt_{cell} , respectively. To account for this, the state \mathbf{x}_r is adjusted to include the GNSS receiver's clock bias, namely δt_{gnss} , as well as the difference between the LTE receiver's clock bias and the first LTE base stations clock bias, namely $(\delta t_{\text{cell}} - \delta t_{\text{cell},1})$. Therefore, the state vector that is estimated becomes $\mathbf{x}_r = [\mathbf{r}_r^\top, c\delta t_{\text{gnss}}, c(\delta t_{\text{cell}} - \delta t_{\text{cell},1})]^\top$. The matrix \mathbf{B} is then adjusted in accordance with this new state to become

$$\mathbf{B} \triangleq \begin{bmatrix} \mathbf{1}_{N \times 1} & \mathbf{0}_{N \times 1} \\ \mathbf{0}_{M \times 1} & \mathbf{1}_{M \times 1} \end{bmatrix}. \quad (6)$$

The weighting matrix in the WNLS is chosen as inverse of the measurement noise covariance $\mathbf{R} = \text{diag}[\sigma_{\text{gnss},1}^2, \dots, \sigma_{\text{gnss},N}^2, \sigma_{\text{cell},1}^2, \sigma_{\text{cell},2}^2 + \sigma_{\epsilon,2}^2, \dots, \sigma_{\text{cell},M}^2 + \sigma_{\epsilon,M}^2]$.

V. SIGNAL RELIABILITY MAP GENERATION

The purpose of signal reliability maps is to find the reliable measurements that can be used by the AGV, and inform the path planning generator (discussed in Section VI) of these measurements. Therefore, signal reliability maps are generated only using information that is known *a priori*, i.e., before the path planning generator prescribes a path to the AGV. Information that is known *a priori* includes 3-D building maps and other static objects in the environment. Information that is not known *a priori* includes pedestrians or other vehicles.

A signal reliability map is a spatiotemporal map specifying for each location in the road network the GNSS satellites to which there is expected to be blocked LOS and the pseudorange multipath error produced for each cellular base station. The following subsections define the signal reliability maps for GNSS and cellular signals and discuss their generation and storage.

A. GNSS Signal Reliability Map Generation

GNSS signals suffer from multipath interference and NLOS conditions in urban environments. Multipath interference in urban environments is a dominant error source to which many mitigation techniques have been proposed [58]–[60]. Receiver-based multipath mitigation techniques typically require the LOS signal to be received [61], while more advanced techniques in NLOS conditions require specialized antennas and additional hardware [62].

The GNSS receiver used in the experiment in the sequel paper [18] used a posteriori multipath estimation (APME+) mitigation technology to subtract multipath interference from GNSS measurements [63]. The proposed approach in this article will only use GNSS satellites that are classified as having clear LOS. To this end, the signal reliability map for GNSS signals stores information about whether the LOS path between the receiver and satellite is obstructed. GNSS visibility prediction using 3-D building maps has been proposed in prior literature [30], [31]. GNSS reliability maps differ from prior work in the way that the visibility information is stored. Since GNSS satellite positions change with time, the GNSS signal reliability maps store the time intervals when a satellite is visible at a given location. The intervals are stored for each satellite and each location.

Formally, the GNSS signal reliability map for a given satellite is a sequence with P elements, where each element represents a location in the road network. The environment consists of N transmitters. The signal reliability map for the n th satellite is

$$\mathcal{M}_{\text{gnss}_n} = \{\mathcal{T}_{\text{gnss}_n, p}\}_{p=1}^P, \quad \text{for } n = 1, \dots, N.$$

Here, p represents a unique index corresponding to a particular location in the road network. Each $\mathcal{T}_{\text{gnss}_n, p}$ is a sequence of ordered pairs representing the start and end times for which the n th satellite has unobstructed LOS at location p , i.e.,

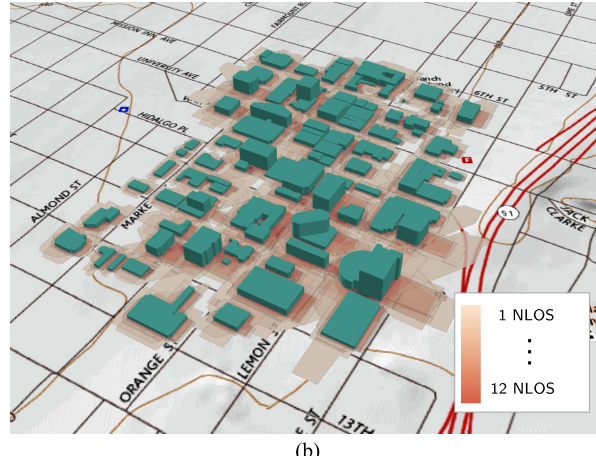
$$\mathcal{T}_{\text{gnss}_n, p} = \{(t_{\text{start}, p, \tau}, t_{\text{end}, p, \tau})\}_{\tau=1}^{T_\tau}.$$

For one day, there are a total of T_τ time intervals with start and end times $t_{\text{start}, p, \tau}$ and $t_{\text{end}, p, \tau}$, respectively. The GNSS signal reliability map could be generated *a priori* and updated periodically (e.g., every day, whenever new ephemerides are available, or whenever the 3-D building map undergoes change). The signal reliability map can be stored locally at the vehicle or at a cloud-hosted database. At a location p , the n th satellite has unobstructed LOS at time t if

$$t_{\text{start}, p, \tau} \leq t \leq t_{\text{end}, p, \tau}, \quad \text{for any } \tau = 1, \dots, T_\tau.$$



(a)



(b)

Fig. 3. Visualization of GNSS signal reliability maps. (a) Region in downtown Riverside, CA, USA, in which signal blockage to a particular GNSS satellite is depicted as a 2-D red polygon. (b) Polygon layers corresponding to 12 different satellites overlayed to generate a “heat-type” map representing the number of satellites to which there is NLOS. This figure is obtained with ArcGIS [49].

The signal reliability maps for N satellites are collectively referred to by $\mathcal{M}_{\text{gnss}} = \{\mathcal{M}_{\text{gnss}_n}\}_{n=1}^N$. Fig. 3 shows a visualization of GNSS signal reliability maps. Here, Fig. 3(a) shows a region in downtown Riverside, CA, USA, in which signal blockage for a particular GNSS satellite is depicted as a 2-D red polygon. Fig. 3(b) overlays the maps of 12 different GNSS satellites to yield a “heat-type” map representing the number of satellites to which there is NLOS.

For a given time, signal reliability maps are visualized as point features, but they can also be visualized as a polygon layer or raster feature. In the simulation and experimental sections in the sequel paper [18], GNSS reliability maps are stored as point features using ArcGIS software [49]. It is worth noting that the proposed approach can be extended to account for GNSS multipath bias by utilizing previously developed algorithms for simulating multipath bias for GNSS signals [30], [59], [64].

Other methods for storing GNSS visibility information can be used. For example, several locations in the road network can store obstruction boundary information known as skymasks, proposed in prior literature [65]. It is expected

that the amount of memory required to store skymasks and GNSS reliability maps is similar. As an example scenario, consider storing reliability maps for GPS and GLONASS satellites (49 active satellites), and that there are three times in one day where the satellite becomes visible on average over each location. The amount of memory required per location is about 900 bytes ($49 \text{ satellites} \times 6 \text{ time values} \times 3 \text{ bytes per time value}$). Then, consider storing skymasks over the same locations. Assume that there are 100 points (200 total elevations and azimuths) stored in a skymask as floats (4 bytes). The amount of memory required per location is 800 bytes ($200 \text{ floats} \times 4 \text{ bytes per float}$). It can be seen that the amount of memory per location is about the same for GNSS reliability masks and skymasks. One advantage for using reliability maps is it will require less computation compared to skymaps, because it only requires checking that a time is within bounds. One disadvantage for using reliability maps is as the number of GNSS satellites increases, the amount of memory for GNSS reliability maps will increase, while the amount of memory for skymasks will stay the same.

B. Cellular Signal Reliability Map Generation

Compared to GNSS signals, cellular signals are often received at lower elevation angles, which make them more susceptible to multipath-induced errors. While multipath mitigation techniques for cellular signals have been an active area of research recently, multipath continues to be among the most dominating sources of error, thereby inducing a large pseudorange measurement bias, especially when the power of the reflected path is higher than the power of the direct path [12], [66].

The cellular signal reliability map stores simulated pseudorange bias caused by multipath. The bias is found using the complex channel impulse response, which provides information about arrival time, phase, and power of each signal path. The complex channel impulse response and the LOS path can be readily calculated using proprietary simulation software (e.g., Wireless Insite [67]). This calculation requires knowledge about the cellular environment, including transmitter location, signal characteristics, antenna type, 3-D building map of the environment, and receiver location. This is carried out for all M cellular transmitters and different receiver locations within the environment. In what follows, the multipath-induced bias calculation from the channel impulse response is discussed.

At each receiver location, the impulse response for the i th LTE OFDM symbol is given by

$$h_i(t) = \sum_{x=0}^{X-1} a_i(x) \delta(\tau - \tau_i(x)) \quad (7)$$

where X is the number of impulses, $a_i(x)$ corresponds to the complex-valued amplitude, and $\tau_i(x)$ is the corresponding path delay. The complex channel impulse response (7) can be used to measure the multipath interference,

$\chi_m \triangleq \chi_{1,m}(i) + \chi_{2,m}(i)$, for $m = 1, \dots, M$, where

$$\begin{aligned} \chi_{1,m}(i) &= A \left| \sum_{l=0}^{L-1} \sum_{x=1}^{X-1} a_i(x) e^{-j2\pi(l/L)(\tau_i(x)/T_s + \tilde{\epsilon}_\theta - \xi)} \right|^2 \\ &\quad - A \left| \sum_{l=0}^{L-1} \sum_{x=1}^{X-1} a_i(x) e^{-j2\pi(l/L)(\tau_i(x)/T_s + \tilde{\epsilon}_\theta + \xi)} \right|^2 \end{aligned} \quad (8)$$

$$\begin{aligned} \chi_{2,m}(i) &= 2A \Re \left[\left(\sum_{l=0}^{L-1} e^{-j2\pi(l/L)(\tilde{\epsilon}_\theta - \xi)} \right) \right] \\ &\quad - 2A \Re \left[\left(\sum_{l=0}^{L-1} e^{-j2\pi(l/L)(\tilde{\epsilon}_\theta + \xi)} \right) \right] \\ &\quad \left(\sum_{l'=0}^{L-1} \sum_{x=1}^{X-1} a_i^*(x) e^{j2\pi(l'/L)(\tau_i(x)/T_s + \tilde{\epsilon}_\theta - \xi)} \right) \end{aligned} \quad (9)$$

where $\Re[\cdot]$ denotes the real part, T_s is the sampling interval, $0 < \xi \leq 0.5$ is the time shift in the LTE receiver's tracking loop ($\xi = 0.5$ is chosen in this article), L is the number of subcarrier symbols in the pilot (200 when the bandwidth is 20 MHz and the cell-specific reference signal is used as the pilot), and A is the signal power due to antenna gain and implementation loss [14], [68]. The theory for (8) and (9) is presented in [68]. The normalized symbol timing error $\tilde{\epsilon}_\theta$ is set to zero to assume perfect tracking. Using (8) and (9), the multipath interference χ_m for all M cellular transmitters is determined.

The multipath-induced bias is comprised of the multipath interference χ_m and the NLOS bias (i.e., path delay between the first received path and the LOS path). That is, the multipath-induced bias is given by

$$b_{m,p} \triangleq \chi_m + c\tau_i(0) - d_{\text{LOS}} \quad (10)$$

where d_{LOS} is the length of the LOS path, therefore, $c\tau_i(0) - d_{\text{LOS}}$ is the NLOS bias. If $|a_i(x)| < \kappa$, for all $x = 0, \dots, X - 1$, where κ is a threshold, the LTE signal is rendered too weak to be tracked and the signal reliability map assumes no cellular measurement at that location. For each cellular transmitter, the bias is stored for each location in the cellular signal reliability map. Formally, the cellular signal reliability map for the m th transmitter is a sequence with P elements

$$\mathcal{M}_{\text{cell}_m} = \{b_{m,p}\}_{p=1}^P$$

where $b_{m,p} = \emptyset$ when the m th cellular measurement is not received at the p th location, where \emptyset denotes null. The signal reliability maps for M LTE transmitters are collectively referred to by $\mathcal{M}_{\text{cell}} = \{\mathcal{M}_{\text{cell}_m}\}_{m=1}^M$.

Fig. 4 shows a visualization of a cellular signal reliability map for a single cellular base station corresponding to the U.S. cellular provider AT&T in downtown Riverside, CA, USA. A raster feature is illustrated, where the black regions indicate that the pseudorange bias due to multipath at the p th location exceeds a threshold $\eta_{\max} = 0.5$ m, i.e., $b_{m,p} \geq 0.5$

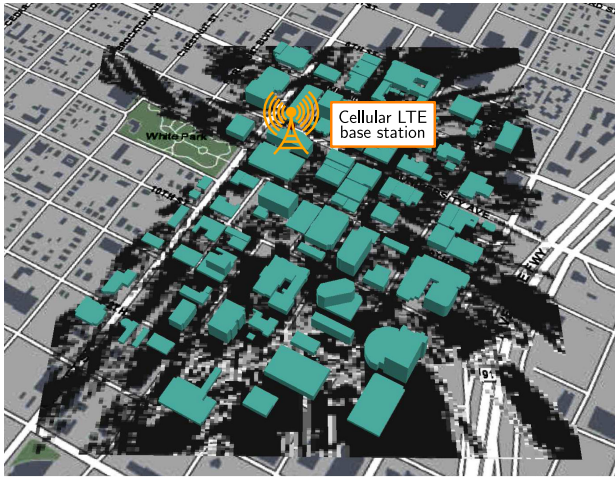


Fig. 4. Visualization of the cellular signal reliability map. The black regions indicate that the pseudorange bias due to multipath at the p th location exceeds a threshold $\eta_{\max} = 0.5$ m, i.e., $b_{m,p} \geq 0.5$ or there is no cellular measurement, i.e., $b_{m,p} = \emptyset$ at the p th position. This figure is obtained with ArcGIS [49].

or there is no cellular measurement, i.e., $b_{m,p} = \emptyset$ at the p th position. The threshold η_{\max} is the pseudorange bias threshold used in the path planning optimization problem explained in Sections VI-B and VII.

C. Thresholding Cellular Signal Reliability Map Analysis

As the LTE wavelength is around 15 cm, a change of a few centimeters in the receiver position can change the relative phase in the complex channel impulse response. The relative phase affects the multipath interference χ_m . In prior work, it was shown that areas where the multipath-induced bias exceeds a threshold can be clustered together [42]. Therefore, a thresholded value of the multipath-induced bias is used instead of the exact simulated value in the path planning uncertainty-based constraint, discussed further in Section VI-B. This subsection studies the validity of simulating and using the thresholded cellular reliability maps. The validity is studied over perturbations in the relative phase in the complex channel impulse response.

The following assumption is studied: if the simulated multipath-induced bias exceeds (or does not exceed) a threshold η_{\max} , then the bias with perturbed relative phases also exceeds (or does not exceed) η_{\max} . This claim is tested by perturbing the multipath interference, i.e., the part of the multipath-induced bias that is affected by phase. The relative phases in several simulated channel impulse responses are perturbed, and the perturbed multipath interference terms are compared to the unperturbed terms. The complex channel impulse responses are calculated with Wireless Insite software, using 3-D building maps from downtown Riverside, CA, USA, shown in Fig. 3. Around 45 600 locations were simulated in the downtown area. For all locations that received more than one path, the relative phases for each path were perturbed according to a uniform distribution from -180° to 180° , and 1000 perturbed multipath interference terms are calculated per location. Five cases for η_{\max} are considered in the results shown in Table I.

TABLE I
Results From Multipath Interference Simulation

	$\eta_{\max} = 1$ meter	$\eta_{\max} = 2$ meters	$\eta_{\max} = 3$ meters	$\eta_{\max} = 4$ meters	$\eta_{\max} = 5$ meters
TP	2447615	2833299	2980151	3066321	3130131
TN	1306398	1075419	974027	910183	861776
FP	241885	161601	140549	128479	122769
FN	240102	165681	141273	131017	121324
TPR	91.07 %	94.48 %	95.47 %	95.90 %	96.27 %
TNR	84.38 %	86.94 %	87.39 %	87.63 %	87.53 %

The metrics in Table I are defined as follows [69].

- 1) True positive (TP) is the number of perturbed terms that do not exceed η_{\max} , while the unperturbed term also does not exceed η_{\max} .
- 2) True negative (TN) is the number of perturbed terms that exceed η_{\max} , while the unperturbed term also exceeds η_{\max} .
- 3) False positive (FP) is the number of perturbed terms that do not exceed η_{\max} , while the unperturbed term exceeds η_{\max} .
- 4) False negative (FN) is the number of perturbed terms that exceed η_{\max} , while the unperturbed term does not exceed η_{\max} .

Table I also provides the true positive rate (TPR) and true negative rate (TNR) [69], given by

$$\text{TPR} = \frac{\text{TP}}{\text{TP} + \text{FN}}, \quad \text{TNR} = \frac{\text{TN}}{\text{TN} + \text{FP}}.$$

TPR corresponds to the percentage of the perturbed terms that are correctly identified as not exceeding η_{\max} . TNR corresponds to the percentage of perturbed terms that are correctly identified as exceeding η_{\max} . It can be seen in Table I that for a threshold as low as 1 m, the percentage of terms that are correctly identified as being below the threshold is 91.07%.

VI. POSITION MSE AND UNCERTAINTY CONSTRAINT CALCULATION

This section describes the formulation of the optimization function and constraints used to generate the optimal path for the AGV to follow. The optimization function involves the position MSE, which is discussed in the first subsection, while the constraint involves the largest eigenvalue of the position estimation error covariance, which is discussed in the second subsection.

In what follows, the biased and unbiased error states are formally defined based on the measurement model and the estimator. Since the measurement model is nonlinear with respect to the state vector \mathbf{x}_r , the model is linearized according to

$$\Delta z_r = \mathbf{H} \Delta \mathbf{x}_r + v$$

where the Δz_r is the measurement error vector, which is the difference between the measurement vector z_r and its estimate \hat{z}_r ; $\Delta \mathbf{x}_r \triangleq \mathbf{x}_r - \hat{\mathbf{x}}_r$, i.e., $\Delta \mathbf{x}_r$ is the estimation error, which is the difference between \mathbf{x}_r and the WNLS estimate

$\hat{\mathbf{x}}_r$; and $\mathbf{v} \triangleq [v_{\text{gnss},1}, \dots, v_{\text{gnss},N}, v_{\text{cell},1}, \dots, v_{\text{cell},M}]^T$. To analyze the effect of multipath-induced bias, a deterministic bias \mathbf{b} is introduced in the measurement

$$\Delta\mathbf{z}_r \triangleq \Delta\mathbf{z}'_r + \mathbf{b}$$

where $\Delta\mathbf{z}'_r = [\Delta\mathbf{z}_{rgnss}^T, \Delta\mathbf{z}_{rcell}^T]^T$ is the unbiased measurement error vector.

The effect of the pseudorange bias on the position estimate can be found through the normal equation (see, for example, [70, (7.67)])

$$\begin{aligned}\Delta\mathbf{x}_r &= (\mathbf{H}^T \mathbf{R}^{-1} \mathbf{H})^{-1} \mathbf{H}^T \mathbf{R}^{-1} \Delta\mathbf{z}_r \\ &= (\mathbf{H}^T \mathbf{R}^{-1} \mathbf{H})^{-1} \mathbf{H}^T \mathbf{R}^{-1} (\Delta\mathbf{z}'_r + \mathbf{b}) \\ &= (\mathbf{H}^T \mathbf{R}^{-1} \mathbf{H})^{-1} \mathbf{H}^T \mathbf{R}^{-1} \Delta\mathbf{z}'_r \\ &\quad + (\mathbf{H}^T \mathbf{R}^{-1} \mathbf{H})^{-1} \mathbf{H}^T \mathbf{R}^{-1} \mathbf{b}.\end{aligned}$$

Therefore, the bias in the pseudorange introduces an additive bias in the estimation error according to

$$\Delta\mathbf{x}_r = \Delta\mathbf{x}'_r + \mathbf{x}_{r,\text{err}}$$

where $\mathbf{x}_{r,\text{err}} \triangleq [\mathbf{r}_{r,\text{err}}^T, c\delta\mathbf{t}_{\text{err}}^T]^T$ results from the multipath-induced bias in the measurement, and $\Delta\mathbf{x}'_r \triangleq [\Delta\mathbf{r}'_r^T, c\Delta\delta\mathbf{t}^T]^T$ is the unbiased state estimation error. The vector $\delta\mathbf{t}$ represents the vector of clock bias states. Therefore, the unbiased state estimation error and the state bias can be, respectively, expressed as

$$\begin{aligned}\Delta\mathbf{x}'_r &= (\mathbf{H}^T \mathbf{R}^{-1} \mathbf{H})^{-1} \mathbf{H}^T \mathbf{R}^{-1} \Delta\mathbf{z}'_r \\ \mathbf{x}_{r,\text{err}} &= (\mathbf{H}^T \mathbf{R}^{-1} \mathbf{H})^{-1} \mathbf{H}^T \mathbf{R}^{-1} \mathbf{b}.\end{aligned}\quad (11)$$

The following subsection explains the steps for using the GNSS and cellular signal reliability maps whose generation was described in Section V to calculate the position MSE for the path planning cost function, and calculate the largest eigenvalue of the position estimation error covariance for the path planning constraint.

A. Position MSE

The position MSE is a scalar measure, which accounts for the precision and bias of an estimator [71], and is commonly used due to its mathematical tractability. It refers to the mean of the squared estimation error in the position at a specified location and time, i.e.,

$$\begin{aligned}\text{3-D position MSE} &= \mathbb{E} [\Delta\mathbf{r}_r^T \Delta\mathbf{r}_r] \\ &= \text{tr} [\mathbb{E} [\Delta\mathbf{r}_r \Delta\mathbf{r}_r^T]] \\ &= \text{tr} [\mathbb{E} [(\Delta\mathbf{r}'_r + \mathbf{r}_{r,\text{err}})(\Delta\mathbf{r}'_r + \mathbf{r}_{r,\text{err}})^T]] \\ &= \text{tr} [\mathbb{E} [\Delta\mathbf{r}'_r \Delta\mathbf{r}'_r^T]] + \|\mathbf{r}_{r,\text{err}}\|_2^2\end{aligned}\quad (12)$$

where $\mathbb{E}[\cdot]$ denotes the expected value and $\text{tr}[\cdot]$ denotes the trace, and (12) follows from $\Delta\mathbf{r}'_r$ being zero-mean. The position bias is $\|\mathbf{r}_{r,\text{err}}\|_2^2$, obtained from the first three elements of $\mathbf{x}_{r,\text{err}}$. The covariance of the unbiased position error is related to the weighted-position dilution of precision (WPDOP) according to [72]

$$\text{WPDOP} \triangleq \sqrt{\text{tr} [\text{cov}[\Delta\mathbf{r}'_r]]}$$

$$= \sqrt{h_{11}^2 + h_{22}^2 + h_{33}^2}$$

where h_{jj} is the j th diagonal of $(\mathbf{H}^T \mathbf{R}^{-1} \mathbf{H})^{-1}$.

The calculation of the position bias $\|\mathbf{r}_{r,\text{err}}\|_2$ due to multipath uses the simulated LOS and pseudorange bias due to multipath, which were found in the signal reliability maps. The steps to calculate the position MSE are described next.

1) *Step 1. Calculate the Vector \mathbf{b} :* For location p and time t , there are $\bar{N} \leq N$ reliable GNSS measurements as determined by the signal reliability maps such that for each $n = 1, \dots, \bar{N}$, where t satisfies a time interval defined in $\mathcal{T}_{\text{gnss},n,p}$. Also, there are $\bar{M} \leq M$ reliable cellular measurements for all $m = 1, \dots, \bar{M}$, such that $b_{m,p}$ is not null and $|b_{m,p}| \leq \eta_m$, where η_m is the m th element of $\mathbf{R}_a^{-T} \mathbf{1}_{(\bar{N}+\bar{M}) \times 1} \eta_{\max}$, where \mathbf{R}_a is the Cholesky factor of \mathbf{R} , i.e., $\mathbf{R} = \mathbf{R}_a^T \mathbf{R}_a$. The method for calculating the threshold η_{\max} is shown in Section VI-B. The pseudorange bias vector is $\mathbf{b} = [\mathbf{0}_{1 \times \bar{N}}, b_{1,p}, \dots, b_{\bar{M},p}]^T$.

2) *Step 2. Calculate the Jacobian \mathbf{H} :* The rows of \mathbf{H} are calculated from the transmitter positions of the corresponding elements in \mathbf{b} , and the coordinates of location p . It is assumed that the biased position and true position are close enough so that the measurement Jacobian for the true position is close to that of the biased position.

3) *Step 3. Calculate the MSE:* The position MSE is calculated from

$$\text{3-D position MSE} \triangleq \text{WPDOP}^2 + \|\mathbf{r}_{r,\text{err}}\|_2^2.$$

The position MSE at a particular position p and time t , denoted $\text{MSE}(p, t)$, will be used in the path planning algorithm described in Section VII.

B. Uncertainty Constraint Calculation

This subsection describes the calculation of the path planning constraint on the largest eigenvalue of the position estimation error covariance. The purpose of this constraint is to restrict the AGV's path to be within the maximum position uncertainty. To this end, the largest eigenvalue of the position-estimation error covariance will be used, which specifies the length of the largest axis of the uncertainty ellipsoid [73]. The largest eigenvalue at a particular position p and at time t , denoted $\lambda_{\max}(p, t)$, is found from the upper 3×3 matrix block of $(\mathbf{H}^T \mathbf{R}^{-1} \mathbf{H})^{-1}$, where \mathbf{H} is calculated according to the method discussed in Section VI-A.

This constraint is also related to a conservative upper bound on the position bias, which can be derived from the expression

$$\mathbf{r}_{r,\text{err}} = (\tilde{\mathbf{G}}^T \tilde{\mathbf{G}})^{-1} \tilde{\mathbf{G}}^T \bar{\mathbf{b}} \quad (13)$$

where

$$\begin{aligned}\tilde{\mathbf{G}} &= (\mathbf{I} - \bar{\mathbf{B}}\Gamma\bar{\mathbf{B}}^T)\tilde{\mathbf{G}}, & \tilde{\mathbf{G}} &= \mathbf{R}_a^{-T}\mathbf{G} \\ \Gamma &= (\bar{\mathbf{B}}^T\bar{\mathbf{B}})^{-1}, & \bar{\mathbf{b}} &= \mathbf{R}_a^{-T}\mathbf{b}, & \bar{\mathbf{B}} &= \mathbf{R}_a^{-T}\mathbf{B}.\end{aligned}$$

The derivation of (13) is given in Appendix A. The bias corresponding to the m th cellular measurement is constrained such that $|b_{m,p}| \leq \eta_m$, where η_m is the m th element of $\mathbf{R}_a^{-T}\mathbf{1}_{(\bar{N}+\bar{M}) \times 1}\eta_{\max}$ and η_{\max} is the pseudorange bias threshold. The constraint can also be written as $|\bar{\mathbf{b}}| \leq \mathbf{1}_{(\bar{N}+\bar{M}) \times 1}\eta_{\max}$, where $|\cdot|$ corresponds to the absolute value of each element in the vector.

Subsequently, the upper bound on the position bias can be found according to

$$\begin{aligned}\|\mathbf{r}_{r,\text{err}}\|_2 &\leq \underset{\|\bar{\mathbf{b}}\|_2 \leq 1\eta_{\max}}{\text{maximize}} \|(\tilde{\mathbf{G}}^T\tilde{\mathbf{G}})^{-1}\tilde{\mathbf{G}}^T\bar{\mathbf{b}}\|_2 \\ &\leq \underset{\|\bar{\mathbf{b}}\|_2 \leq \sqrt{\bar{M}}\eta_{\max}}{\text{maximize}} \|(\tilde{\mathbf{G}}^T\tilde{\mathbf{G}})^{-1}\tilde{\mathbf{G}}^T\bar{\mathbf{b}}\|_2\end{aligned}\quad (14)$$

$$= \underset{\|\bar{\mathbf{b}}\|_2 = \sqrt{\bar{M}}\eta_{\max}}{\text{maximize}} \|(\tilde{\mathbf{G}}^T\tilde{\mathbf{G}})^{-1}\tilde{\mathbf{G}}^T\bar{\mathbf{b}}\|_2 \quad (15)$$

$$= \sqrt{\bar{M}}\eta_{\max} \underset{\|\bar{\mathbf{b}}'\|_2 = 1}{\text{maximize}} \|(\tilde{\mathbf{G}}^T\tilde{\mathbf{G}})^{-1}\tilde{\mathbf{G}}^T\bar{\mathbf{b}}'\|_2 \quad (16)$$

$$= \eta_{\max}\sqrt{\bar{M}}\sigma'_{\max} [(\tilde{\mathbf{G}}^T\tilde{\mathbf{G}})^{-1}\tilde{\mathbf{G}}^T] \quad (17)$$

$$= \eta_{\max}\sqrt{\bar{M} \cdot \lambda_{\max}[(\tilde{\mathbf{G}}^T\tilde{\mathbf{G}})^{-1}]} \triangleq \bar{r}_{\max} \quad (18)$$

where σ'_{\max} denotes the largest singular value, λ_{\max} denotes the largest eigenvalue, and \bar{r}_{\max} denotes the upper bound on the position bias. Equation (14) is found by relaxing the box constraint (i.e., a constraint where the optimization vector, $\bar{\mathbf{b}}$ in this case, has upper and lower thresholds) to a 2-norm ball (i.e., the space bounded by the L^2 -norm), where \bar{M} is the number of cellular measurements used. Equation (15) follows from convexity of the objective function and constraints (i.e., the value of $\|\bar{\mathbf{b}}\|_2$ that maximizes the objective function lies on the boundary of the constraint). Equation (16) is found through change of variables $\bar{\mathbf{b}}' \triangleq \frac{1}{\sqrt{\bar{M}}\eta_{\max}}\bar{\mathbf{b}}$. Equation (17) follows from the definition of the largest singular value. Equation (18) follows from the relationship between the largest eigenvalue and the largest singular value of a matrix. The term $\lambda_{\max}[(\tilde{\mathbf{G}}^T\tilde{\mathbf{G}})^{-1}]$ denotes the maximum eigenvalue of the position estimation error covariance. The upper bound in (18) shows that the maximum eigenvalue also relates to the position error.

C. Simulated Receiver Spacing

This subsection studies the impact of spatial sampling on the position MSE, defined in Section VI-A. The position MSE was calculated over a 209-m path based on simulated LTE and GPS reliability maps. The GPS reliability map was generated on September 20, 2020 at 11:20 UTC. Otherwise, the simulation environment and settings are similar to those defined in the companion paper [18]. Fig. 5 shows the calculated position MSE over various simulated receiver position spacings. The figure also shows the position root-mean-squared error (RMSE) for each spacing, calculated as the root of the average position MSE along the path.

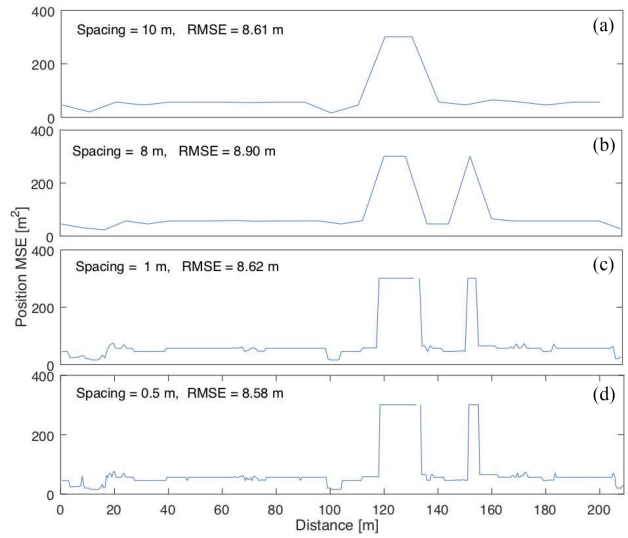


Fig. 5. Position MSE over simulated receiver position spacings of (a) 10 m, (b) 8 m, (c) 1 m, and (d) 0.5 m. A spike in position MSE occurs between distances 151.5 and 155 m, and is captured in (b)–(d).

It can be seen that there is a loss of resolution in the high spacing cases, where the position MSE appears to be smeared compared to the lower resolution cases. In Fig. 5(d), around 150 m, there is a 3.5-m section of high position MSE that is not captured in Fig. 5(a). Despite these differences, the position RMSE averages to a similar value across all spacings to within 0.3 m.

The following conclusions can be drawn as they pertain to path planning metrics. When using position MSE as a path planning cost function, a high spacing (10 m) suffices, as can be shown by the closeness of the position RMSE over the four spacing cases. As a path planning constraint, smaller spacing (1 m) would be preferable to capture the spikes and locations with too few measurements. Methods for improving the sampling method (e.g., based on the amount of surrounding building features) can be explored in future work.

VII. PATH PLANNING GENERATION

The path planning generation step utilizes the signal reliability map to prescribe an optimal path for the AGV to follow. This section describes the steps to determine the optimal path between a start position at a desired departure time and a target position. The optimal path is one that accounts for the shortest path length and the position MSE, subject to a maximum tolerable uncertainty (as measured by the largest eigenvalue of the position estimation error covariance).

To account for both position error and path length, the optimization cost function is chosen to be the sum of the position MSE along the path, multiplied by the distance between two adjacent points. The distance is explicitly considered in the cost function because only including position MSE could result in lengthy paths, e.g., paths that require the AGV to leave and reenter the urban environment. The optimization function constraints account for the position

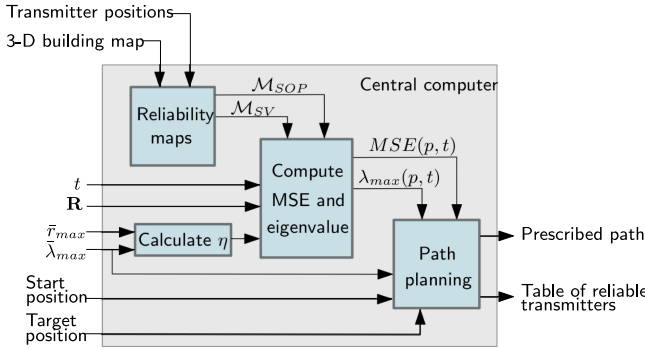


Fig. 6. Flow chart of signal reliability map generation, position MSE and uncertainty constraint calculation, and path planning generation.

bias due to cellular multipath as well as uncertainty about the AGV's position estimate. The user-specified constraints are: threshold for position bias \bar{r}_{\max} and threshold for position uncertainty $\bar{\lambda}_{\max}$. The threshold $\bar{\lambda}_{\max}$ is used as a constraint for all points p and time t along the AGV's path, i.e., $\lambda_{\max}(p, t) \leq \bar{\lambda}_{\max}$. The threshold $\bar{\lambda}_{\max}$ is also used along with \bar{r}_{\max} to calculate a threshold on the pseudorange bias η_{\max} . The calculation of η_{\max} can be achieved from (18) by substituting the user-specified \bar{r}_{\max} , and using $\bar{\lambda}_{\max}$ in place of $\lambda_{\max}[(\tilde{\mathbf{G}}^T \tilde{\mathbf{G}})^{-1}]$. Since $\bar{M} \leq M$, \bar{M} is replaced with M to calculate an upper bound that is independent of a particular location and is valid for the entire environment.

The path planning generation block solves a constrained optimization problem, discussed next, and returns the AGV's prescribed path along with a list of reliable GNSS satellites and cellular base stations to use along the path. As the AGV traverses this optimal path, it only uses signals from these reliable GNSS satellites and cellular base stations. Note that to make the WNLS estimation problem observable, there needs to be at least either $\bar{N} \geq 4$ reliable GNSS satellite signals to estimate $\mathbf{x}'_r \triangleq [\mathbf{r}_r^T, c\delta t_r]^T$ or $\bar{N} + \bar{M} \geq 5$ reliable GNSS satellite and cellular signals to estimate $\mathbf{x}_r \triangleq [\mathbf{r}_r^T, c\delta t_r, c\delta t_{cell,1}]^T$, with $\bar{M} \geq 1$. Fig. 6 summarizes the flowchart of signal reliability map generation, position MSE and eigenvalue calculation, and path planning generation with the corresponding inputs and outputs defined in Sections V and VI.

To account for distance in the optimization problem, each location p is assigned a distance, for $p = 1, \dots, P$. This distance, denoted $\text{dist}(p)$, signifies the length of the road network segment represented by the location p and its adjacent location, and is based on the spatial discretization of the reliability maps. The steps to calculate the distance for locations $p = 1, \dots, P$ are summarized in Fig. 7. Point p_3 in Fig. 7 shows the calculation of $\text{dist}(p_3)$ when the point is adjacent to an intersection, and Point p_2 in Fig. 7 shows the calculation of $\text{dist}(p_2)$ when the point is not adjacent to an intersection. If the street has multiple lanes in one direction, a location index is assigned to each lane, and $\text{dist}(p)$ is assigned the distance shown divided by the number of lanes.

The path planning optimization problem is formulated next. Formally, a path from the start to the target location is denoted $\pi \in \mathcal{P}$, where \mathcal{P} is the set of all paths. The path

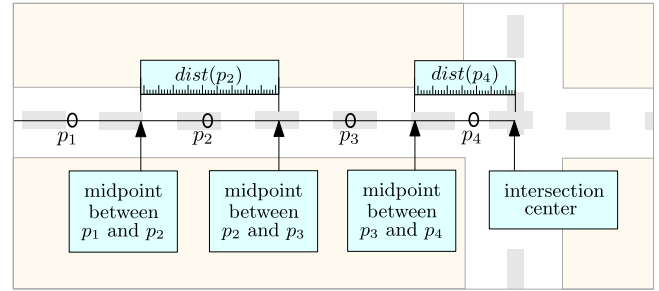


Fig. 7. Steps to calculate $\text{dist}(p)$ for 3-D points whose indices are p_2 and p_4 . For p_4 , which is adjacent to an intersection, the 3-D midpoint between p_4 and p_3 is calculated, then $\text{dist}(p_4)$ is the distance between the midpoint and the intersection center. For p_2 , which is not adjacent to an intersection, the midpoint between p_3 and p_2 is calculated, then the midpoint between p_2 and p_1 is calculated. Then, $\text{dist}(p_2)$ is the distance between the two calculated midpoints.

π is composed of a sequence of position indices between the start position index p_s and the target p_g , namely $\pi = \{p_s, p_1, p_2, \dots, p_g\}$.

The optimization problem is expressed as

$$\begin{aligned} & \underset{\pi \in \mathcal{P}}{\text{minimize}} \quad \sum_{p \in \pi} \text{dist}(p) \cdot \text{MSE}(p, t) \\ & \text{subject to} \quad \lambda_{\max}(p, t) \leq \bar{\lambda}_{\max} \\ & \quad \|\mathbf{r}_{r,\text{err}}\|_2 \leq \bar{r}_{\max}. \end{aligned} \quad (19)$$

The second constraint in (19) can be relaxed using (18) to yield the optimization problem

$$\begin{aligned} & \underset{\pi \in \mathcal{P}}{\text{minimize}} \quad \sum_{p \in \pi} \text{dist}(p) \cdot \text{MSE}(p, t) \\ & \text{subject to} \quad \lambda_{\max}(p, t) \leq \bar{\lambda}_{\max} \\ & \quad |\bar{b}| \leq 1\eta_{\max}. \end{aligned} \quad (20)$$

Note that the cost function in (20) accounts for both the position MSE and the path length. Other cost functions could be used to favor either part: position MSE versus path length, e.g., using an exponential for either term.

The optimization problem (20) resembles the problem of finding the shortest path in a weighted graph, where the roads are the edges of the graph and the path planning metric determines the weight of each edge. Several algorithms have been proposed to find the shortest path that use dynamic programming [74]–[76]. These algorithms cannot be used because the problem lacks optimal substructure due to the time-varying nature of the costs and constraints in (20). The following subsections show two possible approaches for prescribing a path to the AGV.

A. Path Planning Generator: Approach A

To simplify the optimization problem and use dynamic programming for the path planning algorithm, it will be assumed that the GNSS reliability map from the departure time through the time the AGV arrives at the target position is time invariant, making $\text{MSE}(p, t) = \text{MSE}(p)$ and $\lambda_{\max}(p, t) = \lambda_{\max}(p)$. This assumption is reasonable for short AGV paths during which the geometry of the

GNSS satellite constellation does not vary significantly. For example, a GPS satellite moves less than 0.152 radians in 15 min (see Appendix B). An additional check is performed to ensure that the GNSS reliability map does not have sharp changes (i.e., loss of a satellite) as the AGV executes the path, in which case Approach B is to be implemented instead. This check requires the assumption that the vehicle travels at a constant speed v_{AGV} .

Based on the aforementioned assumption, dynamic programming can be used in this approach. Among existing path planning algorithms, Dijkstra's algorithm is most widely used and is recognized as a classic algorithm to find the shortest path between two arbitrary nodes of a weighted graph [77]. Dijkstra's algorithm is readily implementable with acceptable complexity; thus, it is adopted in this approach to solve the AGV path planning problem.

Assume that the AGV is driving in a region consisting of ι intersections and ω roads (e.g., side streets and highways). This region can be modeled by a graph $\mathcal{G} = (\iota, \omega)$, which consists of ι nodes and ω edges. Each intersection corresponds to a node, and each street segment that connects two intersections corresponds to either one or two edges. In the experiments in the companion paper [18], the graph is constructed using the following rules.

- 1) One-way street segments are assigned one edge with one direction.
- 2) Two-way street segments are assigned two edges with one direction for each way.

The path planning metric $f(\beta, \alpha)$ assigns a nonnegative real number corresponding to the weight of the edge from nodes β to α in \mathcal{G} . Based on the objective function in (20), the weight is given by the position MSE at all points from nodes β and α , denoted $P(\beta, \alpha)$, multiplied by $\text{dist}(p)$, i.e.,

$$f(\beta, \alpha) = \sum_{p \in P(\beta, \alpha)} \text{dist}(p) \cdot \text{MSE}(p).$$

It is assumed that the deviation between $\text{MSE}(p)$ and the MSE calculated at the true time is small. Based on the constraints in (20), if $\lambda_{\max}(p)$ exceeds $\bar{\lambda}_{\max}$ for $p \in P(\beta, \alpha)$, then the edge is removed from the graph.

Dijkstra's algorithm is implemented as follows. Let s indicate the start node at which the AGV starts, and let g indicate some target node. Let $d(g)$ denote the cost along the path from s to g , let S denote the set of edges that have already been evaluated by the algorithm, and let V denote the set of unvisited nodes. Within a path $\gamma(g) \in \mathcal{G}$, denote α_p as the predecessor of α and β_p as the predecessor of β . To ensure $\gamma(g)$ does not have loss of a satellite, the algorithm tracks the time of travel from the source to the current node, denoted $t(s, \alpha)$. Approach A is initialized as follows:

- 1) $d(s) = 0$;
- 2) $t(s) = 0$;
- 3) for each node α adjacent to s , set $d(\alpha) = f(s, \alpha)$ and $\alpha_p = s$;
- 4) for each node α such that $\alpha \neq s$ and α is not adjacent to s , set $d(\alpha) = \infty$;

Algorithm 1: Path Planning Algorithm.

Input: \mathcal{G}, s, g, S , and $f(\beta, \alpha)$
Output: $d(g)$ and $\gamma(g)$

- 1: Find $\alpha \in V$ that minimizes $d(\alpha)$
- 2: For each β adjacent to α
- 3: If $d(\alpha) + f(\beta, \alpha) < d(\beta)$,
- 4: $d(\beta) = d(\alpha) + f(\beta, \alpha)$
- 5: $\beta_p = \alpha$
- 6: $t(s, \alpha) = t(s, \alpha) + \text{dist}(\beta, \alpha) \cdot v_{AGV}$
- 7: If satellite becomes obstructed at α between $t(s)$ and $t(s, \alpha)$,
- 8: Exit the Algorithm, goto Approach B
- 10: Else,
- 11: Do not change $d(\beta)$ and β_p
- 12: End if
- 13: End for
- 14: $V \leftarrow V - \{\alpha\}$
- 15: $S \leftarrow S + \{\alpha\}$
- 16: If $S \neq V$,
- 17: Goto Step 1
- 18: Else,
- 19: Exit the Algorithm
- 20: End if

- 5) $S = \{s\}$.

After the aforementioned initialization, the path planning algorithm outlined in Algorithm 1 is executed.

If no paths satisfy the constraint, then the user is made aware that there are no feasible paths with the current settings. To receive ζ admissible paths in addition to the optimal path, Yen's algorithm is used [78]. Yen's algorithm is described in detail in the next subsection. The node and edge data of the graph \mathcal{G} can be extracted from digital maps, such as the Open Street Map (OSM) database [79]. OSM is built by a community of mappers that contribute and maintain roads, trails, and railway stations information.

B. Path Planning Generator: Approach B

For long trajectories spanning long travel time, the optimization problem cannot be simplified as shown in the previous subsection, since the assumption that the reliability map is time-invariant would not hold. Therefore, this subsection considers path planning for long trajectories while accounting for satellite motion.

In this approach, a trajectory is considered long if there is a large change in the geometry of the satellites that are expected to have LOS along the path. The resultant path is determined to be long if either of the following conditions are met.

- 1) The path is long if it is expected to take longer than a threshold time to traverse the path. GPS satellites move less than 0.152 radians in 15 min at high elevation angles (see Appendix B), so we can consider 15 min to be the threshold time. A threshold

distance between the start and target location can be calculated by assuming a constant speed v_{AGV} . Therefore, if the distance between the start and target location exceeds $900 \text{ s} \cdot v_{\text{AGV}}$ (i.e., the total distance travelled by a vehicle moving at speed v_{AGV} for 15 min), Approach B is used.

- 2) The path is considered long based on the check performed in Approach A. If a satellite is expected to lose LOS during the path execution, there will be a large change in the cost function and constraints, and Approach B is used. This check is performed using GNSS reliability maps and assumption of constant speed.

Approach B is implemented as follows. The road network is modeled as a graph \mathcal{G} similar to Approach A, except the edge weights correspond to Euclidean distance, i.e.,

$$f_1(\beta, \alpha) = \sum_{p \in P(\beta, \alpha)} \text{dist}(p).$$

The ζ shortest paths in Euclidean distance are found in the road network using Yen's algorithm [78]. The ζ shortest paths are stored in \mathcal{A} , where each path is denoted as \mathcal{A}^z from $z = 1, \dots, \zeta$. Yen's algorithm exploits the fact that many of the shortest paths will be coincident. This is done by first setting some edge weights to ∞ , then finding the shortest path from a selected node in the k th previous path (called a spur node and denoted α_{spur}) to the target node g . This path from α_{spur} to g , denoted as γ_{spur} , is called the spur path. Then, the new path is calculated by adding the spur path to the k th previous path from s to α_{spur} , called the root path and denoted $\gamma_{\text{rootpath}_k}$. The resulting path is added to set \mathcal{B} , and the shortest path in \mathcal{B} is added to set \mathcal{A} .

The path planning cost along each path in \mathcal{A} is calculated based on the position MSE

$$f_2(\mathcal{A}^z) = \sum_{p \in P(\mathcal{A}^z)} \text{dist}(p) \cdot \text{MSE}(p, t)$$

for $z = 1, \dots, \zeta$, where $P(\mathcal{A}^z)$ is the set of location indices in \mathcal{A}^z . The algorithm returns the path with the smallest $f_2(\mathcal{A}^z)$ that satisfies $\lambda_{\max}(\mathcal{A}^z) > \bar{\lambda}_{\max}$ for $p \in P(\mathcal{A}^z)$ and for all $z = 1, \dots, \zeta$. The constraint $\lambda_{\max}(\mathcal{A}^z)$ is the maximum eigenvalue metric along the entire path \mathcal{A}^z based on the constraints in (20).

After the aforementioned initialization, the path planning algorithm outlined in Algorithm 2, where $\mathcal{A}^z[k]$ is used to denote the k th node in path \mathcal{A}^z .

The computational complexity of Approach B is $O(\zeta t^3)$, which is higher than the computational complexity of Approach A, $O(t^2)$ [78]. Another disadvantage for Approach B is that the prescribed path is not guaranteed to be optimal like in Approach A. However, for trajectories with long duration, Approach B will be more correct because it accounts for satellite motion. Choosing Approach A over Approach B for paths with long duration can lead to worse navigation performance than expected, or ignoring measurements that can be used. This point is discussed further in the sequel paper [18].

Algorithm 2: Path Planning Algorithm.

Input: $\mathcal{G}, s, g, f_1, f_2$
Output: $d(g)$ and $\gamma(g)$

- 1: $\mathcal{A}^1 = \text{Dijkstras}(\mathcal{G}, s, g)$
- 2: $\gamma(g) = \mathcal{A}^1; d(g) = f_2(\mathcal{A}^1)$
- 3: For $z = 2$ to ζ ,
- 4: Create local copy of $\mathcal{G}; \mathcal{B} = \{\}$
- 5: For $k = 1$ to $\text{len}(\mathcal{A}^{z-1}) - 1$
- 6: $\alpha_{\text{spur}} = \mathcal{A}^{z-1}[k]$
- 7: $\gamma_{\text{rootpath}_z} = \mathcal{A}^{z-1}[0 : k]$
- 8: For $j = 1 : z - 1$,
- 9: $\gamma_{\text{rootpath}_j} = \mathcal{A}^j[0 : k]$
- 10: If $\gamma_{\text{rootpath}_z} = \gamma_{\text{rootpath}_j}$,
In \mathcal{G} copy, $f_1(\alpha_{\text{spur}}, \mathcal{A}^j[k + 1]) = \infty$
- 12: End if
- 13: End for
- 14: $\gamma_{\text{spur}} = \text{Dijkstras}(\mathcal{G}, \alpha_{\text{spur}}, g)$
- 15: $\mathcal{B} \leftarrow \mathcal{B} + \{\gamma_{\text{rootpath}_k} + \gamma_{\text{spur}}\}$
- 16: End for
- 17: Sort \mathcal{B}
- 18: If $\lambda_{\max}(\mathcal{B}^1) < \bar{\lambda}_{\max}$ and $f_2(\mathcal{B}^1) > d(g)$
- 19: $\gamma(g) = \mathcal{B}^1; d(g) = f_2(\mathcal{B}^1)$
- 20: End if
- 21: $\mathcal{A} \leftarrow \mathcal{A} + \mathcal{B}^1$
- 22: End for

VIII. CONCLUSION

This article considered the problem where an AGV equipped with GNSS and cellular receivers desires to reach a target location while taking the shortest path with minimum position MSE, while guaranteeing that the bias in the position estimate and the position uncertainty are below desired thresholds. Parameters of the cellular pseudoranges related to the transmitter clock bias are estimated in an initialization step in an open-sky environment. A path planning generator prescribes a trajectory that satisfies this objective using a 3-D building map to create signal reliability maps for GNSS and cellular LTE signals. The signal reliability maps are used to calculate the position MSE and uncertainty-based constraint at each location, which in turn is used to generate an optimal path for the AGV to follow. In Part II of this study, extensive simulation and experimental results are presented demonstrating the improvement in the position RMSE by employing the proposed framework and the consistency between the simulated results with those obtained experimentally on a ground vehicle driving in downtown Riverside, CA, USA.

This article demonstrated the feasibility of using path planning to improve GNSS and cellular positioning, and there are opportunities for future work. Different methods of spatial sampling can be explored, where location indices are distributed based on properties of the road network. Other or additional information can be stored in reliability maps, such as measurement noise variances as a function of simulated carrier-to-noise ratio. Other error sources can be introduced in the path planning cost and constraints,

such as GNSS multipath-induced bias, or inaccuracies in the building footprints that have been modeled in prior work [80]. Methods for GNSS and cellular visibility predictions can be improved through comparing signal availability and received signal strength to 3-D map predictions using power and shadow matching [29], [34], or using a fish-eye camera to detect GNSS NLOS [33]. The same costs and constraints can be evaluated with different navigation frameworks that use filtering techniques and sensor fusion. Integrity monitoring techniques [47] and map matching [48] can also be used to improve transmitter selection or augment the path planning cost function. Time-varying path planning in approach B can be improved by using traffic information [81].

APPENDIX A

RELATIONSHIP BETWEEN PSEUDORANGE AND POSITION BIAS

This appendix establishes the relationship between position bias and pseudorange bias [cf., (13)]. For this analysis, it is assumed that the biased position and true position are close enough so that the measurement Jacobians evaluated at each are approximately equal.

From (11), the relationship between pseudorange bias and the state bias is given by

$$\mathbf{x}_{r,\text{err}} \triangleq (\mathbf{H}^T \mathbf{R}^{-1} \mathbf{H})^{-1} \mathbf{H}^T \mathbf{R}^{-1} \mathbf{b}.$$

Consider the Choleky factorization of $\mathbf{R} = \mathbf{R}_a^T \mathbf{R}_a$, and define $\bar{\mathbf{H}} \triangleq \mathbf{R}_a^{-T} \mathbf{H}$ and $\bar{\mathbf{b}} \triangleq \mathbf{R}_a^{-T} \mathbf{b}$, which results in

$$\mathbf{x}_{r,\text{err}} = (\bar{\mathbf{H}}^T \bar{\mathbf{H}})^{-1} \bar{\mathbf{H}}^T \bar{\mathbf{b}}. \quad (21)$$

Recall that $\mathbf{H} \triangleq [\mathbf{G}, \mathbf{B}]$ and $\mathbf{x}_{r,\text{err}} \triangleq [r_{r,\text{err}}^T, c\delta t_{\text{err}}^T]^T$; therefore, (21) can be partitioned as

$$\begin{bmatrix} \mathbf{r}_{r,\text{err}} \\ c\delta t_{\text{err}} \end{bmatrix} = \begin{bmatrix} \bar{\mathbf{G}}^T \bar{\mathbf{G}} & \bar{\mathbf{G}}^T \bar{\mathbf{B}} \\ \mathbf{B}^T \bar{\mathbf{G}} & \bar{\mathbf{B}}^T \bar{\mathbf{B}} \end{bmatrix}^{-1} \begin{bmatrix} \bar{\mathbf{G}}^T \\ \bar{\mathbf{B}}^T \end{bmatrix} \bar{\mathbf{b}}.$$

An expression for $\mathbf{r}_{r,\text{err}}$ can be found through block matrix inversion

$$\begin{aligned} \mathbf{r}_{r,\text{err}} &= \begin{bmatrix} \mathbf{A} & -\mathbf{A}\bar{\mathbf{G}}^T \bar{\mathbf{B}}\Gamma \end{bmatrix} \begin{bmatrix} \bar{\mathbf{G}}^T \\ \bar{\mathbf{B}}^T \end{bmatrix} \bar{\mathbf{b}} \\ \mathbf{A} &\triangleq (\bar{\mathbf{G}}^T \bar{\mathbf{G}} - \bar{\mathbf{G}}^T \bar{\mathbf{B}}\Gamma \bar{\mathbf{B}}^T \bar{\mathbf{G}})^{-1} \end{aligned} \quad (22)$$

where $\Gamma = (\bar{\mathbf{B}}^T \bar{\mathbf{B}})^{-1}$. After rearranging (22), the relationship is found to be

$$\begin{aligned} \mathbf{r}_{r,\text{err}} &= (\bar{\mathbf{G}}^T \bar{\mathbf{G}} - \bar{\mathbf{G}}^T \bar{\mathbf{B}}\Gamma \bar{\mathbf{B}}^T \bar{\mathbf{G}})^{-1} (\bar{\mathbf{G}}^T - \bar{\mathbf{G}}^T \bar{\mathbf{B}}\Gamma \bar{\mathbf{B}}^T) \bar{\mathbf{b}} \\ &= (\bar{\mathbf{G}}^T (\mathbf{I} - \bar{\mathbf{B}}\Gamma \bar{\mathbf{B}}^T) \bar{\mathbf{G}})^{-1} \bar{\mathbf{G}}^T (\mathbf{I} - \bar{\mathbf{B}}\Gamma \bar{\mathbf{B}}^T) \bar{\mathbf{b}} \end{aligned}$$

where $(\mathbf{I} - \bar{\mathbf{B}}\Gamma \bar{\mathbf{B}}^T)$ is a projection matrix. The aforementioned equation can be rewritten as

$$\mathbf{r}_{r,\text{err}} = (\tilde{\mathbf{G}}^T \tilde{\mathbf{G}})^{-1} \tilde{\mathbf{G}}^T \bar{\mathbf{b}}$$

where $\tilde{\mathbf{G}} \triangleq (\mathbf{I} - \bar{\mathbf{B}}\Gamma \bar{\mathbf{B}}^T) \bar{\mathbf{G}}$.

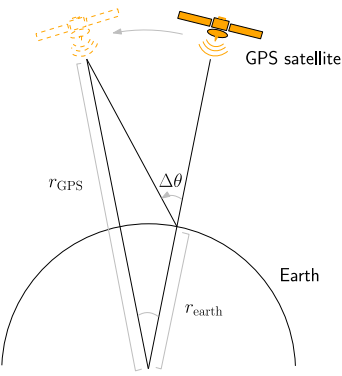


Fig. 8. Description of the variables used to approximate the change in satellite geometry.

APPENDIX B

CHANGE IN GNSS SATELLITE GEOMETRY

This appendix provides an approximation of the change in satellite geometry as a function of time. For a conservative approximation, the GNSS satellite is assumed to start at zenith, where the angular velocity from the surface of Earth is fastest. GNSS satellite angular velocities, denoted ω_s , can be used. For example, for a GPS satellite $\omega_s \approx 1.522 \text{ rad/s}$. For low to medium orbit altitudes, the magnitude of the tangential velocity of the satellite in the ECEF shows small variation and can be approximated by a constant [82]. If the satellite starts at zenith, the amount of time T_{GPS} it takes for the GPS satellite to travel $\Delta\theta$ radians can be approximated by

$$T_{\text{GPS}} \approx \frac{2}{\omega_s - \omega_E \cos i} \cos^{-1} \left(\frac{r_{\text{earth}}}{r_{\text{GPS}}} \sin \Delta\theta - \frac{\pi}{2} + \Delta\theta \right) \quad (23)$$

where $r_{\text{earth}} \approx 6371 \text{ km}$ is the radius of Earth, $\omega_E \approx 7.2921 \times 10^{-5} \text{ rad/s}$ is the Earth's angular speed, $i = 55^\circ$ is the inclination angle of the GPS satellite, and $r_{\text{GPS}} \approx 26571 \text{ km}$ is the altitude of the GPS satellite. Equations (23) can be used to calculate the time it takes for the satellite to travel $\Delta\theta$ radians (see Fig. 8).

REFERENCES

- [1] 44 Corporations Working on Autonomous Vehicles, CBInsights, New York, NY, USA, May 2017.
- [2] T. Carone
Self-Driving car accidents will keep happening. We need to learn from them
Mar. 2018. [Online]. Available: <https://money.cnn.com/2018/03/21/technology/self-driving-cars-opinion/index.html?sr=fbmoney032118self-driving-cars-opinion0631AMStory>
- [3] R. Ioannides, T. Pany, and G. Gibbons
Known vulnerabilities of global navigation satellite systems, status, and potential mitigation techniques
Proc. IEEE, vol. 104, no. 6, pp. 1174–1194, Feb. 2016.
- [4] N. Zhu, J. Marais, D. Betaille, and M. Berbineau
GNSS position integrity in urban environments: A review of literature
IEEE Trans. Intell. Transp. Syst., vol. 19, no. 9, pp. 2762–2778, Sep. 2018.

- [5] J. Petit, B. Stottelaar, M. Feiri, and F. Kargl
Remote attacks on automated vehicles sensors: experiments on camera and LiDAR
In *Proc. Black Hat Europe*, 2015, vol. 11, pp. 1–13.
- [6] D. Borio and C. Odriscolll
Design of a general pseudolite pulsing scheme
IEEE Trans. Aerosp. Electron. Syst., vol. 50, no. 1, pp. 2–16, Jan. 2014.
- [7] C. Yang and T. Nguyen
Tracking and relative positioning with mixed signals of opportunity
J. Inst. Navigat., vol. 62, no. 4, pp. 291–311, Dec. 2015.
- [8] Z. Kassas, J. Khalife, K. Shamaei, and J. Morales
I hear, therefore I know where I am: Compensating for GNSS limitations with cellular signals
IEEE Signal Process. Mag., vol. 34, no. 5, pp. 111–124, Sep. 2017.
- [9] C. Yang, T. Nguyen, and E. Blasch
Mobile positioning via fusion of mixed signals of opportunity
IEEE Aerosp. Electron. Syst. Mag., vol. 29, no. 4, pp. 34–46, Apr. 2014.
- [10] M. Driusso, C. Marshall, M. Sabathy, F. Knutti, H. Mathis, and F. Babich
Vehicular position tracking using LTE signals
IEEE Trans. Veh. Technol., vol. 66, no. 4, pp. 3376–3391, Apr. 2017.
- [11] J. Khalife and Z. Kassas
Navigation with cellular CDMA signals—Part II: Performance analysis and experimental results
IEEE Trans. Signal Process., vol. 66, no. 8, pp. 2204–2218, Apr. 2018.
- [12] K. Shamaei, J. Khalife, and Z. Kassas
Exploiting LTE signals for navigation: Theory to implementation
IEEE Trans. Wireless Commun., vol. 17, no. 4, pp. 2173–2189, Apr. 2018.
- [13] J. del Peral-Rosado, J. López-Salcedo, F. Zanier, and G. Seco-Granados
Position accuracy of joint time-delay and channel estimators in LTE networks
IEEE Access, vol. 6, pp. 25185–25199, Apr. 2018.
- [14] K. Shamaei and Z. Kassas
LTE receiver design and multipath analysis for navigation in urban environments
J. Inst. Navigat., vol. 65, no. 4, pp. 655–675, Dec. 2018.
- [15] J. Khalife and Z. Kassas
Precise UAV navigation with cellular carrier phase measurements
In *Proc. IEEE/ION Position, Location, Navigat. Symp.*, Apr. 2018, pp. 978–989.
- [16] K. Shamaei and Z. Kassas
Sub-meter accurate UAV navigation and cycle slip detection with LTE carrier phase
In *Proc. ION GNSS Conf.*, Sep. 2019, pp. 2469–2479.
- [17] S. Ragothaman
Path planning for autonomous ground vehicles using GNSS and cellular LTE signal reliability maps and GIS 3-D maps
Master's thesis, Univ. California, Riverside, CA, USA, 2018.
- [18] S. Ragothaman, M. Maaref, and Z. Kassas
Autonomous ground vehicle path planning in urban environments using GNSS and cellular signals reliability maps: Simulation and experimental results
IEEE Trans. Aerosp. Electron. Syst., to be published.
- [19] A. Davison
Real-time simultaneous localisation and mapping with a single camera
in *Proc. IEEE Int. Conf. Comput. Vis.*, 2003, vol. 2, pp. 1403–1410.
- [20] R. Valencia, M. Morta, J. Andrade-Cetto, and J. Porta
Planning reliable paths with pose SLAM
IEEE Trans. Robot., vol. 29, no. 4, pp. 1050–1059, Aug. 2013.
- [21] M. Mora and J. Tornero
Predictive and multirate sensor-based planning under uncertainty
IEEE Trans. Intell. Veh., vol. 16, no. 3, pp. 1493–1504, Jun. 2015.
- [22] C. Hubmann, J. Schulz, M. Becker, D. Althoff, and C. Stiller
Automated driving in uncertain environments: Planning with interaction and uncertain maneuver prediction
IEEE Trans. Intell. Veh., vol. 3, no. 1, pp. 5–17, Mar. 2018.
- [23] Y. Zheng, Y. Zhang, and L. Li
Reliable path planning for bus networks considering travel time uncertainty
IEEE Intell. Transp. Syst. Mag., vol. 8, no. 1, pp. 35–50, Jan. 2016.
- [24] Z. Tang and U. Ozguner
Motion planning for multitarget surveillance with mobile sensor agents
IEEE Trans. Robot., vol. 21, no. 5, pp. 898–908, Oct. 2005.
- [25] A. Shem, T. Mazzuchi, and S. Sarkan
Addressing uncertainty in UAV navigation decision-making
IEEE Trans. Aerosp. Electron. Syst., vol. 44, no. 1, pp. 295–313, Jan. 2008.
- [26] X. Zhou, X. Yu, and X. Peng
UAV collision avoidance based on varying cells strategy
IEEE Trans. Aerosp. Electron. Syst., vol. 55, no. 4, pp. 1743–1755, Aug. 2019.
- [27] J. Garcia, J. Farrell, Z. Kassas, and M. Ouimet
Autonomous surface vehicle multistep look-ahead measurement location planning for optimal localization of underwater acoustic transponders
IEEE Trans. Aerosp. Electron. Syst., vol. 55, no. 6, pp. 2836–2849, Dec. 2018.
- [28] Z. Kassas and T. Humphreys
Receding horizon trajectory optimization in opportunistic navigation environments
IEEE Trans. Aerosp. Electron. Syst., vol. 51, no. 2, pp. 866–877, Apr. 2015.
- [29] S. Saab and Z. Kassas
Power matching approach for GPS coverage extension
IEEE Trans. Intell. Transp. Syst., vol. 7, no. 2, pp. 156–166, Jun. 2006.
- [30] Y. Lee, Y. Suh, and R. Shibasaki
Ajax GIS application for GNSS availability simulation
J. Civil Eng., vol. 11, no. 6, pp. 303–310, Nov. 2007.
- [31] J. Bradbury, M. Ziebart, P. Cross, P. Boulton, and A. Read
Code multipath modelling in the urban environment using large virtual reality city models: Determining the local environment
J. Navigat., vol. 60, no. 1, pp. 95–105, 2007.
- [32] J. Isaacs, A. Irish, F. Qutin, U. Madhow, and J. Hespanha
Bayesian localization and mapping using GNSS SNR measurements
in *Proc. IEEE/ION Position, Location, Navigat. Symp.*, May 2014, pp. 445–451.
- [33] T. Suzuki and N. Kubo
N-LOS GNSS signal detection using fish-eye camera for vehicle navigation in urban environments
In *Proc. ION GNSS Conf.*, Sep. 2014, pp. 1897–1906.
- [34] L. Wang, P. Groves, and M. Ziebart
Smartphone shadow matching for better cross street GNSS positioning in urban environments
J. Navigat., vol. 69, no. 3, pp. 411–433, 2015.
- [35] L. Hsu, Y. Gu, and S. Kamijo
3D building model-based pedestrian positioning method using GPS/GLONASS/QZSS and its reliability calculation
GPS Solutions, vol. 3, pp. 413–428, 2016.

- [36] J. Isaacs *et al.* GPS-optimal micro air vehicle navigation in degraded environments in *Proc. Amer. Control Conf.*, Jun. 2014, pp. 1864–1871.
- [37] S. Ackermann, A. Angrisano, S. Pizzo, S. Gaglione, C. Gioia, and S. Troisi Digital surface models for GNSS mission planning in critical environments *J. Surveying Eng.*, vol. 140, no. 2, pp. 1–11, 2013.
- [38] A. Nowak Dynamic GNSS mission planning using DTM for precise navigation of autonomous vehicles *J. Navigat.*, vol. 70, no. 3, pp. 483–504, May 2017.
- [39] A. Shetty and G. Gao Predicting state uncertainty for GNSS-based UAV path planning using stochastic reachability in *Proc. ION GNSS Conf.*, 2019, pp. 131–139.
- [40] H. Karimi and D. Asavasuthirakul A novel optimal routing for navigation systems-services based on global navigation satellite system quality of service *J. Intell. Transp. Syst.*, vol. 18, no. 3, pp. 286–298, May 2014.
- [41] G. Zhang and L. Hsu A new path planning algorithm using a GNSS localization error map for UAVs in an urban area *J. Intell. Robotic Syst.*, vol. 94, pp. 219–235, 2019.
- [42] S. Ragothaman, M. Maaref, and Z. Kassas Multipath-optimal UAV trajectory planning for urban UAV navigation with cellular signals in *Proc. IEEE Veh. Technol. Conf.*, Sep. 2019, pp. 1–6.
- [43] K. Shamaei, J. Morales, and Z. Kassas A framework for navigation with LTE time-correlated pseudo-range errors in multipath environments in *Proc. IEEE Veh. Technol. Conf.*, Apr. 2019, pp. 1–6.
- [44] M. Ulmschneider and C. Gentner Multipath assisted positioning for pedestrians using LTE signals in *Proc. IEEE/ION Position, Location, Navigat. Symp.*, Apr. 2016, pp. 386–392.
- [45] A. Abdallah and Z. Kassas Evaluation of feedback and feedforward coupling of synthetic aperture navigation with LTE signals in *Proc. IEEE Veh. Technol. Conf.*, Sep. 2019, pp. 1–6.
- [46] F. Peyret, D. Betaille, P. Carolina, R. Toledo-Moreo, A. Gomez-Skarmeta, and M. Ortiz GNSS autonomous localization: NLOS satellite detection based on 3-D maps *IEEE Robot. Autom. Mag.*, vol. 21, no. 1, pp. 57–63, Mar. 2014.
- [47] M. Maaref and Z. Kassas Measurement characterization and autonomous outlier detection and exclusion for ground vehicle navigation with cellular signals *IEEE Trans. Intell. Veh.*, vol. 5, no. 4, pp. 670–683, Dec. 2020.
- [48] Z. Kassas, M. Maaref, J. Morales, J. Khalife, and K. Shamaei Robust vehicular localization and map matching in urban environments through IMU, GNSS, and cellular signals *IEEE Intell. Transp. Syst. Mag.*, vol. 12, no. 3, pp. 36–52, Jun. 2020.
- [49] ESRI [Online]. Available: <https://www.arcgis.com>.
- [50] Z. Kassas, V. Ghadiok, and T. Humphreys Adaptive estimation of signals of opportunity in *Proc. ION GNSS Conf.*, Sep. 2014, pp. 1679–1689.
- [51] J. Morales and Z. Kassas Optimal collaborative mapping of terrestrial transmitters: Receiver placement and performance characterization *IEEE Trans. Aerosp. Electron. Syst.*, vol. 54, no. 2, pp. 992–1007, Apr. 2018.
- [52] 3GPP Evolved universal terrestrial radio access (E-UTRA); requirements for support of radio resource management *3rd Generation Partnership Project (3GPP)*, TS 36.133, Apr. 2010.
- [53] J. Khalife and Z. Kassas Evaluation of relative clock stability in cellular networks in *Proc. ION GNSS Conf.*, Sep. 2017, pp. 2554–2559.
- [54] P. Misra and P. Enge Global Positioning System: Signals, Measurements, and Performance, 2nd ed., Lincoln, MA: Ganga-Jamuna Press, 2010.
- [55] Z. Kassas and T. Humphreys Observability analysis of collaborative opportunistic navigation with pseudorange measurements *IEEE Trans. Intell. Transp. Syst.*, vol. 15, no. 1, pp. 260–273, Feb. 2014.
- [56] J. Khalife, K. Shamaei, and Z. Kassas Navigation with cellular CDMA signals—Part I: Signal modeling and software-defined receiver design *IEEE Trans. Signal Process.*, vol. 66, no. 8, pp. 2191–2203, Apr. 2018.
- [57] J. Khalife and Z. Kassas Opportunistic UAV navigation with carrier phase measurements from asynchronous cellular signals *IEEE Trans. Aerosp. Electron. Syst.*, vol. 56, no. 4, pp. 3285–3301, Aug. 2020.
- [58] N. Ziedan Urban positioning accuracy enhancement utilizing 3-D buildings model and accelerated ray tracing algorithm in *Proc. ION GNSS Conf.*, Sep. 2017, pp. 3253–3268.
- [59] N. Kbayer and M. Sahmoudi Performances analysis of GNSS NLOS bias correction in urban environment using a three-dimensional city model and GNSS simulator *IEEE Trans. Aerosp. Electron. Syst.*, vol. 54, no. 4, pp. 1799–1814, Feb. 2018.
- [60] J. Lesouple, T. Robert, M. Sahmoudi, J. Tourneret, and W. Vigneau Multipath mitigation for GNSS positioning in an urban environment using sparse estimation *IEEE Trans. Intell. Transp. Syst.*, vol. 20, no. 4, pp. 1316–1328, Apr. 2019.
- [61] N. Jardak, A. Vervisch-Picois, and N. Samama Multipath insensitive delay lock loop in GNSS receivers *IEEE Trans. Aerosp. Electron. Syst.*, vol. 47, no. 4, pp. 2590–2609, Oct. 2011.
- [62] L. Heng, T. Walter, P. Enge, and G. Gao GNSS multipath and jamming mitigation using high-mask-angle antennas and multiple constellations *IEEE Trans. Intell. Transp. Syst.*, vol. 16, no. 2, pp. 741–750, Apr. 2015.
- [63] J. Sleewaegen and F. Boon Mitigating short delay multipath: A promising new technique in *Proc. ION Int. Tech. Meeting Conf.*, Sep. 2010, pp. 204–213.
- [64] D. Roongpiboonsopt and H. Karimi Integrated GNSS QoS prediction for navigation services in *Proc. ACM SIGSPATIAL Int. Workshop Comput. Transp. Sci.*, Nov. 2013, pp. 73–78.
- [65] L. Wang, P. Groves, and M. Ziebart GNSS shadow matching: Improving urban positioning accuracy using a 3D city model with optimized visibility scoring scheme *J. Inst. Navigat.*, vol. 60, no. 3, pp. 195–207, 2013.
- [66] M. Huang and W. Xu Enhanced LTE TOA/OTDOA estimation with first arriving path detection in *Proc. IEEE Wireless Commun. Netw. Conf.*, Apr. 2013, pp. 3992–3997.
- [67] Remcom Dec. 2018. [Online]. Available: <https://www.remcom.com>

- [68] B. Yang, K. Letaief, R. Cheng, and Z. Cao
Timing recovery for OFDM transmission
IEEE J. Sel. Areas Commun., vol. 18, no. 11, pp. 2278–2291, Nov. 2000.
- [69] T. Hastie, R. Tibshirani, and J. Friedman
Elements of Statistical Learning: Data Mining, Inference, and Prediction., New York, NY, USA: Springer, 2009.
- [70] E. Kaplan and C. Hegarty
Understanding GPS: Principles and Applications, 2nd ed. Norwood, MA, USA: Artech-House, 2005.
- [71] S. Kay
Fundamentals of Statistical Signal Processing: Estimation Theory. Upper Saddle River, NJ, USA: Prentice-Hall, 1993.
- [72] D. Won
et al. Weighted DOP with consideration on elevation-dependent range errors of GNSS satellites
IEEE Trans. Instrum. Meas., vol. 61, no. 12, pp. 3241–3250, Dec. 2012.
- [73] Z. Kassas, A. Arapostathis, and T. Humphreys
Greedy motion planning for simultaneous signal landscape mapping and receiver localization
IEEE J. Sel. Topics Signal Process., vol. 9, no. 2, pp. 247–258, Mar. 2015.
- [74] O. G. Swathi and S. Hemamalini
Prims-aided Dijkstra algorithm for adaptive protection in microgrids
IEEE Trans. Emerg. Sel. Topics Power Electron., vol. 4, no. 4, pp. 1279–1286, Dec. 2016.
- [75] P. Hart, N. Nilsson, and B. Raphael
A formal basis for the heuristic determination of minimum cost paths
IEEE Trans. Syst. Sci. Cybern., vol. 4, no. 2, pp. 100–107, Jul. 1968.
- [76] E. Dijkstra
A note on two problems in connexion with graphs
Numerische Mathematik, vol. 1, no. 1, pp. 269–271, Dec. 1959.
- [77] J. Zhang *et al.*
Vehicle routing in urban areas based on the oil consumption weight-Dijkstra algorithm
IET Intell. Transport Syst., vol. 10, no. 7, pp. 495–502, Sep. 2016.
- [78] J. Yen
An algorithm for finding shortest routes from all source nodes to a given destination in general networks
Quart. Appl. Math., vol. 27, no. 1, pp. 526–530, 1970.
- [79] Open Street Map Foundation (OSMF) [Online]. Available: <https://www.openstreetmap.org>
- [80] H. Fan, A. Zipf, Q. Fu, and P. Neis
Quality assessment for building footprints data on OpenStreetMap
Int. J. Geographical Inf. Sci., vol. 28, no. 4, pp. 700–719, 2014.
- [81] E. Nikolova
High-performance heuristics for optimization in stochastic traffic engineering problems
in Proc. Large-Scale Sci. Comput., Jun. 2010, pp. 352–360.
- [82] I. Ali, N. Al-Dhahir, and J. Hershey
Doppler characterization for LEO satellites
IEEE Trans. Commun., vol. 46, no. 3, pp. 309–313, Mar. 1998.



Sonya Ragothaman (Member, IEEE) received the B.S. and M.S. degrees in electrical engineering from the University of California, Riverside, CA, USA, in 2016 and 2018, respectively.

She is an Engineer with Aerospace Corporation, El Segundo, CA. She was a Researcher with the Autonomous Systems Perception, Intelligence, and Navigation Laboratory, from 2016 to 2018. Her research interests include software-in-the-loop model development for launch vehicle flight software, high fidelity simulation of global navigation satellite systems, and satellite pose estimation.



Mahdi Maaref received the B.S. and M.S. degrees from the University of Tehran, Tehran, Iran, in 2008 and 2011, respectively, and the Ph.D. degree in electrical engineering from Shahid Beheshti University, Tehran, in 2016.

He is a Principal Engineer with OneNav, Palo Alto, CA, USA, and was a Postdoctoral Research Fellow with the University of California, Irvine, CA, and a member of the Autonomous Systems Perception Intelligent and Navigation Laboratory, from 2016 to 2020. He was a Visiting Research Collaborator with the University of Alberta, Edmonton, Canada, in 2016. His research interests include autonomous ground vehicles, opportunistic perception, and autonomous integrity monitoring.



Zaher (Zak) M. Kassas (Senior Member, IEEE) received the B.E. degree in electrical engineering from the Lebanese American University, Beirut, Lebanon, the M.S. degree in electrical and computer engineering from The Ohio State University, Columbus, OH, USA, and the M.S.E. degree in aerospace engineering and the Ph.D. degree in electrical and computer engineering from the University of Texas at Austin, Austin, TX, USA.

He is an Associate Professor with the University of California, Irvine, CA, USA, and the Director with the Autonomous Systems Perception, Intelligence, and Navigation (ASPIN) Laboratory. He is also the Director of the U.S. Department of Transportation Center: CARMEN (Center for Automated Vehicle Research with Multimodal AssurEd Navigation), focusing on navigation resiliency and security of highly automated transportation systems. His research interests include cyber-physical systems, estimation theory, navigation systems, autonomous vehicles, and intelligent transportation systems.

Dr. Kassas was the recipient of the 2018 National Science Foundation Faculty Early Career Development Program (CAREER) award and 2019 Office of Naval Research Young Investigator Program award. He was also the recipient of the 2018 IEEE Walter Fried Award, 2018 Institute of Navigation (ION) Samuel Burka Award, and 2019 ION Col. Thomas Thurlow Award. He is an Associate Editor for the IEEE TRANSACTIONS ON AEROSPACE AND ELECTRONIC SYSTEMS and the IEEE TRANSACTIONS ON INTELLIGENT TRANSPORTATION SYSTEMS.